Chapter 10

Dynamo models of the solar cycle

We can add to our knowledge, but we cannot subtract from it.

Arthur Koestler
The Sleepwalkers (1959)

Was einmal gedacht wurde,
kann nicht mehr zurückgenommen werden.

Friedrich Dürrenmatt
Die Physiker (1962)

The time has now come to put everything (well... almost) we have learned so far to construct dynamo models for solar and stellar magnetic fields. In this chapter we concentrate on the Sun, for which the amount of observational data available constrains dynamo models to a degree much greater than for other stars, to the extent that the latter will be considered in a separate, subsequent chapter.

We restrict ourselves here to axisymmetric mean-field-like models, in the sense that we will be setting and solving partial differential equations for poloidal and toroidal large-scale magnetic components, and subsume the effects of small-scale fluid motions and magnetic fields into coefficients of these PDEs:

$$\frac{\partial A}{\partial t} = \underbrace{\eta\left(\nabla^2 - \frac{1}{\varpi^2}\right)A}_{\text{resistive decay}} - \underbrace{\frac{\mathbf{u}_p}{\varpi}\cdot\nabla(\varpi A)}_{\text{advection}} \qquad [+\text{ Source}]\ , \tag{10.1}$$

$$\frac{\partial B}{\partial t} = \underbrace{\eta\left(\nabla^2 - \frac{1}{\varpi^2}\right)B}_{\text{resistive decay}} + \underbrace{\frac{1}{\varpi}\frac{\partial(\varpi B)}{\partial r}\frac{\partial \eta}{\partial r}}_{\text{diamagnetic transport}} - \underbrace{\varpi\mathbf{u}_p\cdot\nabla\left(\frac{B}{\varpi}\right)}_{\text{advection}}$$

$$- \underbrace{B\nabla\cdot\mathbf{u}_p}_{\text{compression}} + \underbrace{\varpi(\nabla\times(A\hat{\mathbf{e}}_\phi))\cdot\nabla\Omega}_{\text{shearing}}\ . \tag{10.2}$$

As you will hopefully recall (cf. §1.12.3), these two PDEs result from the separation of the MHD induction equation upon substitution of axisymmetric flow and magnetic fields having the general form:

$$\mathbf{u}(r,\theta) = \mathbf{u}_p(r,\theta) + \varpi\Omega(r,\theta)\hat{\mathbf{e}}_\phi\ , \tag{10.3}$$

$$\mathbf{B}(r,\theta,t) = \nabla \times (A(r,\theta,t)\hat{\mathbf{e}}_\phi) + B(r,\theta,t)\hat{\mathbf{e}}_\phi \ . \tag{10.4}$$

You will also recall that the presence of a "[Source]" term in eq. (10.1), usually taken to depend on the toroidal field B, is essential for sustained dynamo action, in order to bypass Cowling's theorem (§7.4). With the poloidal source a function of B we recover a nice reciprocal symmetry between eqs. (10.1) and (10.2); the toroidal field production is proportional to the poloidal field strength via the differential rotation. The poloidal field production, in turn, is proportional to the toroidal field strength via the as-yet unspecified poloidal source term; schematically,

$$\nabla\Omega \otimes A \rightarrow B \ , \tag{10.5}$$

$$[\text{Source}] \otimes B \rightarrow A \ , \tag{10.6}$$

where the symbol "$\otimes$" and "$\rightarrow$" stand for "acting on" and "produces". Evidently we have here —at least conceptually— the ingredients needed for self-regeneration (and exponential growth) of both A and B[1]. It will often prove useful to envision dynamo action as the two-step process as outlined above; even though both mechanisms operate simultaneously and concurrently, it is quite possible that they in fact do so in spatially distinct regions of the solar interior, in which case a suitable transport mechanism must exist to link the two source regions.

Moreover, you will certainly also recall (if not `goto` Fig. 6.12 and `return`) that the sun's poloidal magnetic component, as measured on photospheric magnetograms, flips polarity near sunspot cycle maximum, which —presumably— corresponds to the epoch of peak internal toroidal field strength. The poloidal component (P), in turn, peaks at time of sunspot minimum. The cyclic regeneration of the sun's full large-scale field can thus be thought of as a temporal sequence of the form

$$A(+) \rightarrow B(-) \rightarrow A(-) \rightarrow B(+) \rightarrow A(+) \rightarrow \dots \ , \tag{10.7}$$

where the $(+)$ and $(-)$ refer to the signs of the poloidal and toroidal components, as established observationally. The dynamo problem can thus be broken into two sub-problems: generating a toroidal field from a pre-existing poloidal component, and a poloidal field from a pre-existing toroidal component.

With shearing by differential rotation taking care of the $A \rightarrow B$ step, the whole game will hinge on the specification of the poloidal source term in eq. (10.1). The mean-field electrodynamics approach of the preceding chapter is one, mathematically formal way to calculate possible forms (the "α-effect", where [Source]$\equiv \alpha B$), but there exist also some more empirical approaches that we will look into in due time.

Indeed, the different types of dynamo models we will consider in what follows differ primarily in the choice they make regarding the physical origin and mathematical form of this poloidal source term. They all share the shearing of a poloidal field by differential rotation (§7.2.3) as a source of toroidal field, and all invoke some sort of enhanced, "turbulent" magnetic diffusivity in the solar convective envelope (the "β-effect" of the preceding chapter).

For the sake of convenience, we first (§10.1) collect and review these various common model ingredients. We then consider (§10.2) solar cycle models based on simple formulations for the α-effect of mean-field electrodynamics. We then look into what currently stands as their main "competitors", namely solar cycle models based on poloidal field regeneration by the surface decay of active regions, more succinctly known as Babcock-Leighton models (§10.3). We then consider (§10.4) cycle models relying on various MHD instabilities to provide a poloidal source term. We then look into the nonlinear behavior and response to stochastic forcing of some of these models (§10.5), with an eye on understanding some of the observed pattern of solar cycle fluctuations reviewed in chap. 6. We close with a brief survey of the current state of model-based solar cycle prediction schemes (§10.6).

[1] Can you see the similarity here with the mode of operation of the Roberts Cell dynamo, discussed two chapter ago?

10.1 Basic model design

10.1.1 The differential rotation

For the differential rotation $\Omega(r,\theta)$ we retain our now familiar solar-like parametrization (see also Figure 7.12), scaled in terms of the surface equatorial rotation rate:

$$\Omega(r,\theta) = \Omega_C + \frac{\Omega_S(\theta) - \Omega_C}{2}\left[1 + \mathrm{erf}\left(\frac{r - r_C}{w}\right)\right] , \tag{10.8}$$

where

$$\Omega_S(\theta) = (1 - a_2\cos^2\theta - a_4\cos^4\theta) \tag{10.9}$$

with parameter values $\Omega_C = 0.939$, $a_2 = 0.1264$, $a_4 = 0.1591$, $r_c/R = 0.7$, and $w/R = 0.05$, as inferred helioseismologically. Figure 10.1 below shows the corresponding isocontours of angular velocity, together with radial cuts at the pole, equator and mid-latitudes.

It should be noted once again that such a solar-like differential rotation profile is quite complex from the point of view of dynamo modelling, in that it is characterized by *three* partially overlapping shear regions: a strong positive radial shear in the equatorial regions of the tachocline, an even stronger negative radial shear in its polar regions, and a significant latitudinal shear throughout the convective envelope and extending partway into the tachocline. As shown on panel B of Fig. 10.1, for a tachocline of half-thickness $w/R_\odot = 0.05$, the mid-latitude latitudinal shear at $r/R_\odot = 0.7$ is comparable in magnitude to the equatorial radial shear; its potential contribution to dynamo action should not be casually dismissed.

10.1.2 The total magnetic diffusivity

For the total magnetic diffusivity $\eta(r)$ we use the same error-function radial profile as before, normalized to the turbulent diffusivity in the convective envelope:

$$\frac{\eta(r)}{\eta_e} = \Delta\eta + \frac{1 - \Delta\eta}{2}\left[1 + \mathrm{erf}\left(\frac{r - r_c}{w}\right)\right] . \tag{10.10}$$

The corresponding profile is plotted on Fig. 10.1 as a dash-dotted line. In practice, the core-to-envelope diffusivity ratio $\Delta\eta \equiv \eta_c/\eta_e$ is treated as a model parameter, with of course $\Delta\eta \ll 1$, since we associate η_c with the microscopic magnetic diffusivity, and η_e with the presumably much larger mean-field turbulent diffusivity β [2]. With the microscopic diffusivity $\eta_c \sim 1\,\mathrm{m^2 s^{-1}}$ below the core-envelope interface, and taking the mean-field estimates of β at face value, one obtains $\Delta\eta \sim 10^{-9}$—10^{-6}. The solutions discussed below have $\Delta\eta = 10^{-3}$—10^{-1}, which is much larger, but still small enough to nicely illustrate some important consequence of radial gradients in diffusivity.

10.1.3 The meridional circulation

Meridional circulation is unavoidable in turbulent, compressible rotating convective shells. It basically results from an imbalance between Reynolds stresses and buoyancy forces. The $\sim 15\,\mathrm{m\ s^{-1}}$ poleward flow observed at the surface has been detected helioseismically, down to $r/R_\odot \simeq 0.85$ without significant departure from the poleward direction (except locally and very close to the surface, in the vicinity of active region belts). Mass conservation evidently requires an equatorward flow deeper down.

For all models discussed below including a meridional circulation $\mathbf{u}_p(r,\theta)$, we use the following convenient parametric form:

$$u_r(r,\theta) = 2u_0\left(\frac{R}{r}\right)^2\left[-\frac{1}{m+1} + \frac{c_1}{2m+1}\xi^m - \frac{c_2}{2m+p+1}\xi^{m+p}\right]$$

[2] We should perhaps repeat that this assumption is a somewhat dubious one, that moreover has been called into question by direct numerical simulation.

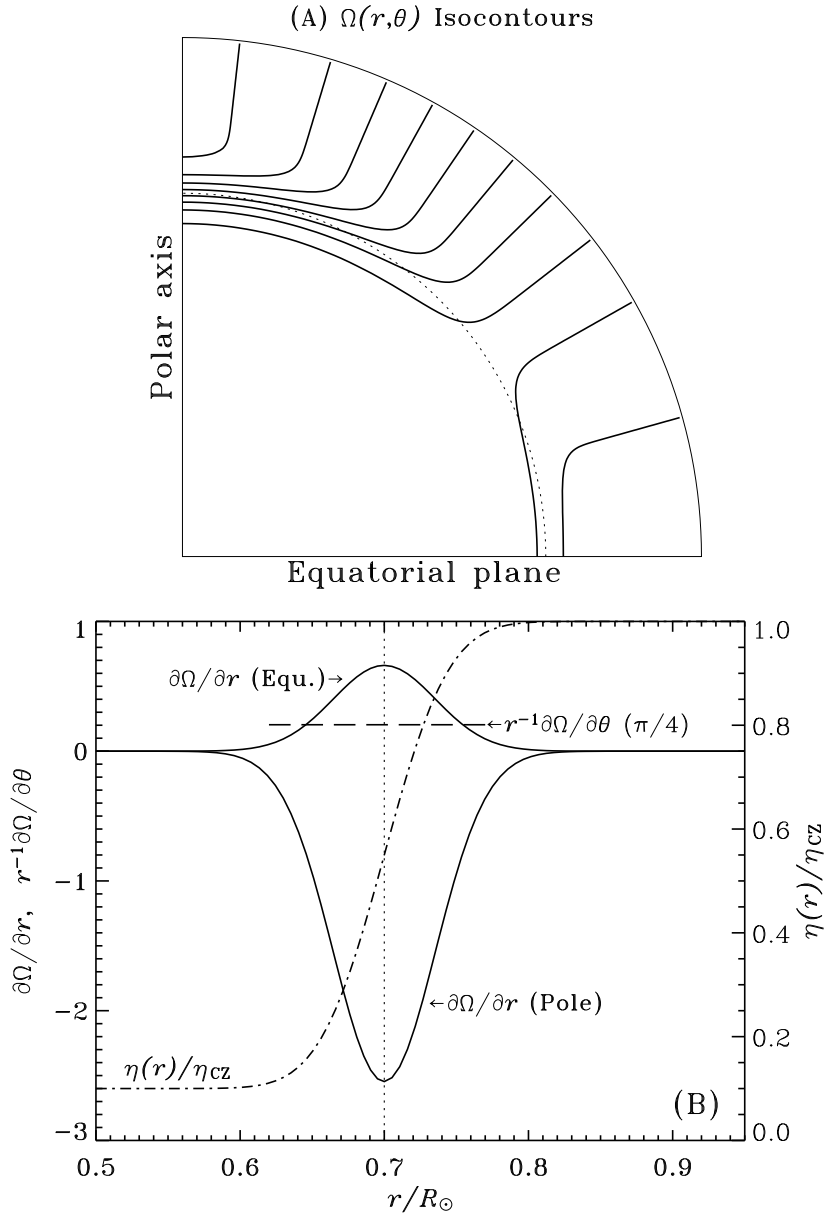

Figure 10.1: Isocontours of angular velocity generated by eqs. (10.8)—(10.9), with parameter values $w/R = 0.05$, $\Omega_C = 0.8752$, $a_2 = 0.1264$, $a_4 = 0.1591$ (panel A). The radial shear changes sign at colatitude $\theta = 55°$. Panel B shows the corresponding angular velocity gradients, together with the total magnetic diffusivity profile defined by eq. (10.10) (dash-dotted line, here with $\Delta\eta = 0.1$ for illustrative purposes). The core-envelope interface is located at $r/R_\odot = 0.7$ (dotted lines).

$$\times\xi[(q+2)\cos^2\theta - \sin^2\theta]\sin^q\theta \ , \tag{10.11}$$

$$u_\theta(r,\theta) = 2u_0\left(\frac{R}{r}\right)^3\left[-1 + c_1\xi^m - c_2\xi^{m+p}\right]\sin^{q+1}\cos\theta \ , \tag{10.12}$$

with

$$c_1 = \frac{(2m+1)(m+p)}{(m+1)p}\xi_b^{-m} \ , \tag{10.13}$$

$$c_2 = \frac{(2m+p+1)m}{(m+1)p}\xi_b^{-(m+p)} \ , \tag{10.14}$$

$$\xi = \frac{R}{r} - 1 \ , \tag{10.15}$$

$$\xi_b = \frac{R}{r_b} - 1 \ . \tag{10.16}$$

This meridional flow satisfies mass conservation ($\nabla\cdot(\rho\mathbf{u}_p) = 0$) for a polytropic density profile of the form:

$$\frac{\rho(r)}{\rho_b} = \left(\frac{R}{r} - 1\right)^m \ . \tag{10.17}$$

Setting $m = 0.5$, $p = 0.25$ and $q = 0$, this defines a steady quadrupolar circulation pattern, with a single flow cell per quadrant extending from the surface down to a depth r_b. Circulation streamlines are shown on Fig. 10.2, together with radial cuts of the latitudinal component at mid-latitudes ($\theta = \pi/4$). The flow is poleward in the outer convection zone, with an equatorward return flow peaking slightly above the core-envelope interface, and rapidly vanishing below.

10.2 Mean-field models

In this section we consider a series of dynamo models where the poloidal source is the (scalar) α-effect of mean-field electrodynamics: For the time being we also restrict the models to the kinematic regime, i.e., all flow fields posed *priori* and deemed steady ($\partial/\partial t = 0$), as described by the functional forms given in §10.1. Unless specifically stated otherwise, we assume the parameter values:

$$\eta_T = 5\times10^7\,\mathrm{m^2\,s^{-1}} \ , \qquad \Delta\eta = 0.1 \ , \tag{10.18}$$

$$\Omega_{\rm eq} = 2.6\times10^{-6}\,\mathrm{rad^2\,s^{-1}} \ , \tag{10.19}$$

which leads to

$$C_\Omega = 2.5\times10^4 \ , \tag{10.20}$$

$$\tau = \frac{R^2}{\eta_T} = 10^{10}\,\mathrm{s} \simeq 300\,\mathrm{yr} \ . \tag{10.21}$$

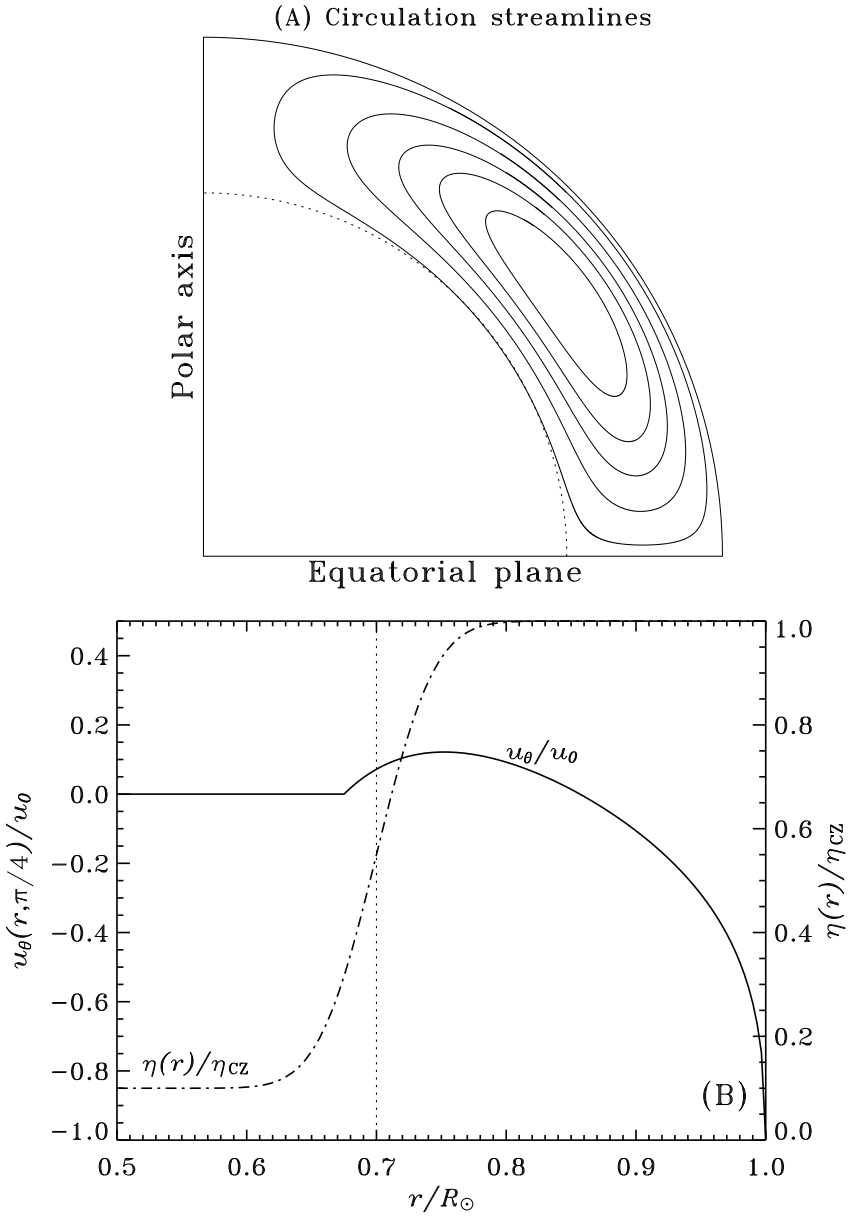

Figure 10.2: Streamlines of meridional circulation (panel A), together with the total magnetic diffusivity profile defined by eq. (10.10) (dash-dotted line, again with $\Delta\eta = 0.1$) and a mid-latitude radial cut of u_θ (bottom panel). The dotted line is the core-envelope interface. This is the analytic flow of van Ballegooijen and Choudhuri (see bibliography), with parameter values $m = 0.5$, $p = 0.25$, $q = 0$ and $r_b = 0.675$.

10.2.1 The $\alpha\Omega$ dynamo equations

In constructing mean-field dynamos for the sun, it has been a common procedure to neglect meridional circulation, on the grounds that it is a very weak flow (but more on this further below), and to adopt the $\alpha\Omega$ model formulation, on the grounds that with $R \simeq 7 \times 10^8\,\mathrm{m}$, $\Omega_0 \sim 10^{-6}\,\mathrm{rad\ s^{-1}}$, and $\alpha_0 \sim 1\,\mathrm{m\ s^{-1}}$, one finds $C_\alpha/C_\Omega \sim 10^3$, independently of the assumed (and poorly constrained) value for η_T. Using the non-dimensional scalings already introduced in §9.4, equations (10.1)—(10.2) then reduce to the so-called $\alpha\Omega$ dynamo equations:

$$\frac{\partial A}{\partial t} = \left(\nabla^2 - \frac{1}{\varpi^2}\right) A + C_\alpha B \ , \tag{10.22}$$

$$\frac{\partial B}{\partial t} = \left(\nabla^2 - \frac{1}{\varpi^2}\right) B + C_\Omega \varpi (\nabla \times A)\cdot(\nabla\Omega) \ . \tag{10.23}$$

In the spirit of producing a model that is solar-like we use a fixed value $C_\Omega = 2.5\times 10^4$, obtained assuming $\Omega_0 = \Omega_{Eq}\Omega_S(0) \sim 10^{-6}\,\mathrm{rad\ s^{-1}}$ and $\eta_0 = 5 \times 10^7\,\mathrm{m^2 s^{-1}}$.

In the parameter regime characterizing the strongly turbulent solar convection zone, the strength (or even sign) of the α-effect cannot be computed in any reliable manner from first principles, so this will remain the major unknown of the model. In accordance with the $\alpha\Omega$ approximation of the dynamo equations, we restrict ourselves to cases where $|C_\alpha| \ll C_\Omega$. For the dimensionless functional $\alpha(r,\theta)$ we use an expression of the form

$$\alpha(r,\theta) = f(r)g(\theta) \ , \tag{10.24}$$

where

$$f(r) = \frac{1}{4}\left[1 + \mathrm{erf}\left(\frac{r-r_c}{w}\right)\right]\left[1 - \mathrm{erf}\left(\frac{r-0.8}{w}\right)\right] \ . \tag{10.25}$$

This combination of error functions concentrates the α-effect in the bottom half of the envelope, and let it vanish smoothly below, just as the net magnetic diffusivity does (i.e., we again set $r_c/R = 0.7$ and $w/R = 0.05$). Various lines of argument point to an α-effect peaking at the bottom of the convective envelope, since there the convective turnover time is commensurate with the solar rotation period, a most favorable setup for the type of toroidal field twisting at the root of the α-effect. Likewise, the hemispheric dependence of the Coriolis force suggests that the α-effect should be positive in the Northern hemisphere, and change sign across the equator ($\theta = \pi/2$). The "minimal" latitudinal dependency is thus

$$g(\theta) = \cos\theta \ . \tag{10.26}$$

The C_α dimensionless number, measuring the strength of the α-effect, is treated as a free parameter of the model. You may be shocked by the fact that we are, in a very very cavalier manner, effectively treating the α-effect as a (almost) free-function; this sorry situation is unfortunately the rule rather than the exception in mean-field dynamo modelling[3].

10.2.2 Linear dynamo solutions

With α, β and the large-scale flow given, The $\alpha\Omega$ dynamo equations (10.22)—(10.23) become linear in the mean-field $\mathbf{B}$. With none of the PDE coefficients depending explicitly on time, one can seek eigensolutions of the form

$$\begin{bmatrix} A(r,\theta,t) \\ B(r,\theta,t) \end{bmatrix} = \begin{bmatrix} a(r,\theta) \\ b(r,\theta) \end{bmatrix} e^{\lambda t} \ , \tag{10.27}$$

[3]References to some of the more noteworthy exceptions are provided in the bibliography at the end of this chapter.

where the amplitudes a and b are in general complex quantities. Substituting eqs. (10.27) into the dynamo equations yields a classical linear eigenvalue problem. The problem being linear, such eigensolutions leave the absolute scale of the magnetic field strength undetermined. It will prove convenient to write the eigenvalue explicitly as

$$\lambda = \sigma + i\omega \ , \tag{10.28}$$

so that σ is the growth rate and ω the cyclic frequency, both expressed in terms of the inverse diffusion time[4] $\tau^{-1} = \eta/R^2$. In a model for the (oscillatory) solar dynamo, we are looking for solutions where $\sigma > 0$ and $\omega \neq 0$. You may think of a dynamo as a peculiar form of MHD instability!

Armed (and dangerous) with the above model, we plow ahead and solve the $\alpha\Omega$ as an eigenvalue problem, using inverse iteration (see appendix F). We first produce a sequence of solutions for increasing values of $|C_\alpha|$, holding C_Ω fixed at a its "solar" value 2.5×10^4, and without meridional circulation ($\mathrm{R}_m = 0$)[5]. Figure 10.3 shows the variation of the growth rate σ and frequency ω as a function of C_α. Four sequences are shown, corresponding to modes that are either antisymmetric or symmetric with respect to the equatorial plane ("A" and "S" respectively), computed with either positive or negative C_α. For $|C_\alpha|$ smaller than some threshold value, the induction terms make too small a contribution to the RHS of eq. (10.22), leaving the dissipation terms dominant, so that solutions all have $\sigma < 0$, as per Cowling's theorem. As $|C_\alpha|$ increases, the growth rate eventually reaches $\sigma = 0$. At this point we also have $\omega \neq 0$, so that the corresponding solution oscillates with neither growth of decay of its amplitude. Further increases of $|C_\alpha|$ lead to $\sigma > 0$. We are now finally in the dynamo regime, where a weak initial field is amplified exponentially in time.

Computing similar sequences for the same same model but different values of C_Ω soon reveals than the onset of dynamo activity ($\sigma > 0$) is controlled by the *product* of C_α and C_Ω:

$$D \equiv C_\alpha \times C_\Omega = \frac{\alpha_0 \Omega_0 R^3}{\eta_0^2} \ . \tag{10.29}$$

The value of D for which $\sigma = 0$ is called the **critical dynamo number** (denoted D_{crit})[6]. This, at least, is similar to what we found for the analytical solution of §9.3[7] Modes having $\sigma < 0$ are called **subcritical**, and those having $\sigma > 0$ **supercritical**. Note on Fig. 10.3 how little the growth rate and dynamo frequency depend on the assumed solution parity.

Here the first mode to become supercritical is the negative C_α mode, for which $D_{\mathrm{crit}} = -0.9 \times 10^5$, followed shortly by the positive C_α mode ($D_{\mathrm{crit}} = -1.1 \times 10^5$). The dynamo frequency for these critical modes is $\omega \simeq 300$, which corresponds to a full cycle period of $\sim 6\,\mathrm{yr}$. This is within a factor of three of the observed full solar cycle period. Once again we should not be too impressed by this, since we have quite a bit of margin of manoeuver in specifying numerical values for η_0 and C_α, and there is no reason to believe that the Sun should be exactly exactly at the critical threshold for dynamo action.

Figure 10.4 shows a half a cycle of the dynamo solution, in the form snapshot of the toroidal (color scale) and poloidal eigenfunctions (fieldlines) in a meridional plane, with the rotation/symmetry axis oriented vertically. The four frames are separated by a phase interval $\varphi = \pi/3$, so that panel (D) is identical to (A) except for reversed magnetic polarities in both magnetic components.

The toroidal field peaks in the vicinity of the core-envelope interface, which is not surprising since in view of eqs. (10.8)—(10.9) the radial shear is maximal there and the magnetic diffusivity

[4] In view of our discussion in chapter 3, this then implies that all mean-field dynamo models produced by solution of eq. (10.27) are *by definition* slow dynamos. Can you figure that one out?

[5] Obtaining such sequences by inverse iteration is easy if one uses the eigenvalue obtained for a given value of C_α as a guess for the eigenvalue of the next solution incremented in C_α. The first eigenvalue of the sequence must be hunted down by trial and error, or estimated using a different numerical technique.

[6] Can you find a way of scaling the $\alpha\Omega$ dynamo equations so that the only nondimensional number appearing in the scaled version of the equation is the dynamo number D defined above?

[7] ...but does not hold for $\alpha^2\Omega$ dynamo solutions!

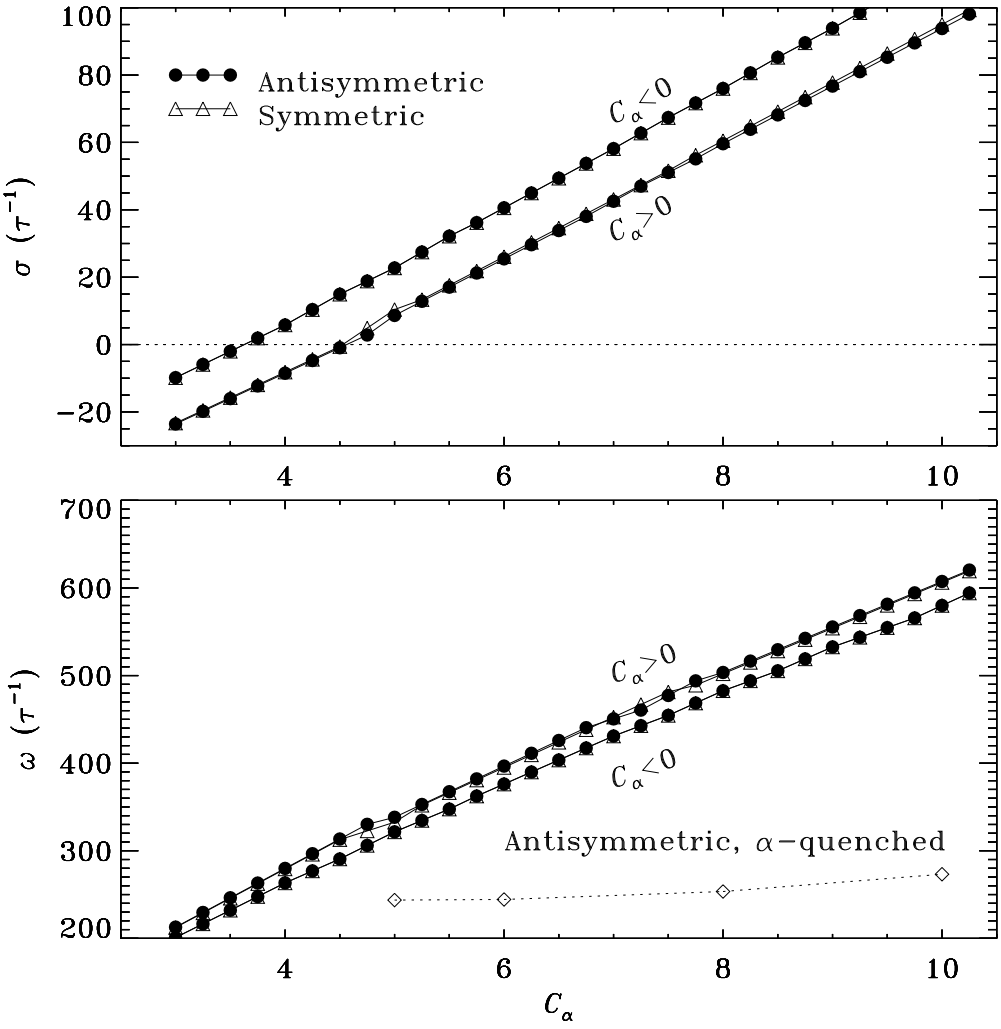

Figure 10.3: Variations of the dynamo growth rate (A) and frequency (B) as a function of increasing $|C_\alpha|$ in the minimal $\alpha\Omega$ model. Sequences are shown for either positive or negative dynamo number (as labeled), and symmetric (triangles) or antisymmetric (dots) parity. Modes having $\sigma < 0$ are decaying, and modes with $\sigma > 0$ exponentially growing. Here modes with A or S parity have very nearly identical eigenvalues. In this model the first mode to reach criticality is the negative C_α mode, for which $D_{\rm crit} = -0.9 \times 10^5$. The positive C_α mode reaches criticality at $D_{\rm crit} = 1.1 \times 10^5$. The diamonds on panel (B) correspond to the dynamo frequency measured in a nonlinear version of the same minimal $\alpha\Omega$ model, including algebraic α-quenching, to be discussed in §10.2.4.

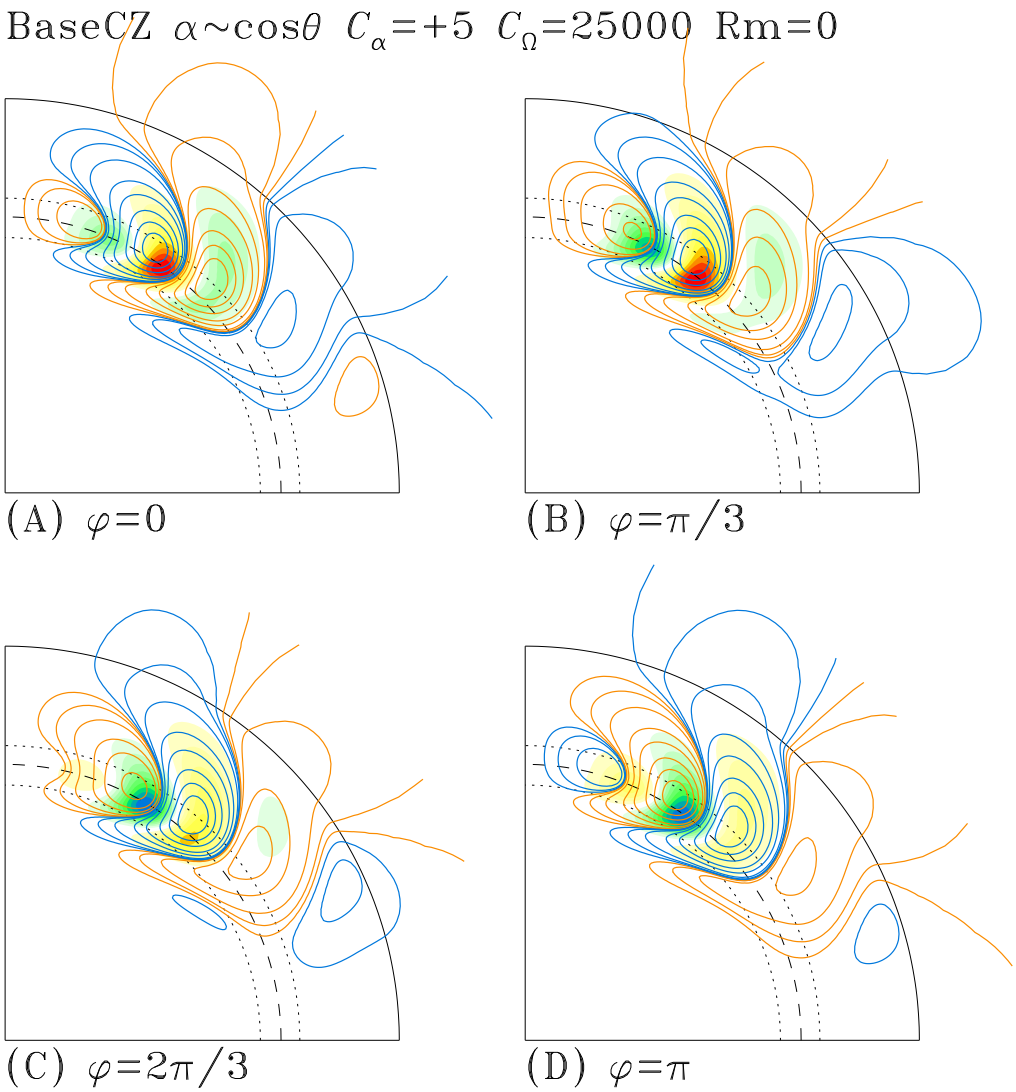

Figure 10.4: Four snapshots in meridional planes of our minimal linear $\alpha\Omega$ dynamo solution with defining parameters $C_\Omega = 25000$, $\eta_T/\eta_c = 10$, $\eta_T = 5 \times 10^7\,\mathrm{m}^2\ \mathrm{s}^{-1}$. With $C_\alpha = +5$, this is a mildly supercritical solution (cf. Fig. 10.3). The toroidal field is plotted as filled contours (green to blue for negative B, yellow to red for positive B, normalized to the peak strength and with increments $\Delta B = 0.2$), on which poloidal fieldlines are superimposed (blue for clockwise-oriented fieldlines, orange for counter-clockwise orientation). The dashed line is the core-envelope interface at $r_c/R = 0.7$. The four snapshots shown here cover a half magnetic cycle, i.e., panel (D) is identical to (A) except for reversed magnetic polarities.

and α-effect are undergoing their fastest variation with depth. But why is the amplitude of the dynamo mode vanishing so rapidly below the core-envelope interface? After all, the poloidal and toroidal diffusive eigenmodes investigated in §7.1 were truly global, and the diamagnetic effect should favor stronger fields in the lower diffusivity core. The crucial difference lies with the oscillatory nature of the solution: because the magnetic field produced in the vicinity of the core-envelope interface is oscillating with alternating polarities, its penetration depth in the core is limited by the electromagnetic skin depth $\ell = \sqrt{2\eta_c/\omega}$ (§7.3), with η_c the core diffusivity. Having assumed $\eta_T = 5 \times 10^7\,\mathrm{m^2 s^{-1}}$, we have $\eta_c = \eta_T \Delta\eta = 5 \times 10^4\,\mathrm{m^2 s^{-1}}$. A dimensionless dynamo frequency $\omega \simeq 300$ corresponds to $3 \times 10^{-8}\,\mathrm{s^{-1}}$, so that $\ell/R \simeq 0.026$, quite small indeed.

Careful examination of 10.4A→D also reveals that the toroidal/poloidal flux systems polarity present in the shear layer first show up at high-latitutes, and then *migrate equatorward* to finally disappear at mid-latitudes in the course of the half-cycle[8]. If you haven't already guessed it, what we are seeing on Figure 10.4 is the spherical equivalent of the dynamo waves investigated in §9.3 for the cartesian case with uniform α-effect and shear, if we identify r with z and x with θ. In more general terms, the dynamo wave travel in a direction $\mathbf{s}$ given by

$$\mathbf{s} = \alpha \nabla\Omega \times \hat{\mathbf{e}}_\phi \ , \tag{10.30}$$

i.e., along isocontours of angular velocity. This result is known as the "Parker-Yoshimura sign rule".

10.2.3 Nonlinearities and α-quenching

Obviously the exponential growth characterizing supercritical ($\sigma > 0$) linear solutions must stop once the Lorentz force associated with the growing magnetic field becomes dynamically significant for the inductive flow. This magnetic backreaction can show up here in two distinct ways:

1. Reduction of the differential rotation,

2. Reduction of turbulent velocities, and therefore of the α-effect (and perhaps also of the turbulent magnetic diffusivity).

Because the solar surface and internal differential rotation shows very little dependence on the phase of the solar cycle, it has been costumary to assume that magnetic backreaction occurs at the level of the α-effect. In the mean-field spirit of *not* solving dynamical equations for the small-scales, it has been standard practice to *assume* a dependence of α on B that "does the right thing", namely reducing the α-effect once the magnetic field becomes "strong enough", the latter usually taken to mean when the growing dynamo-generated mean magnetic field reaches a magnitude such that its energy per unit volume is comparable to the kinetic energy of the underlying turbulent fluid motions. Denoting this **equipartition field strength** by $B_{\rm eq}$, one often introduces an *ad hoc* nonlinear dependency of α (and sometimes η_T as well) directly on the mean-toroidal field B by writing:

$$\alpha \to \alpha(B) = \frac{\alpha_0}{1 + (B/B_{\rm eq})^2} \ . \tag{10.31}$$

Needless to say, this remains an *extreme* oversimplification of the complex interaction between flow and field that is known to characterize MHD turbulence, but its wide usage in solar dynamo modeling makes it a nonlinearity of choice for the illustrative purpose of this section.

[8] An animation of this solution, as well as the one discussed next, can be viewed on the course Web Page.

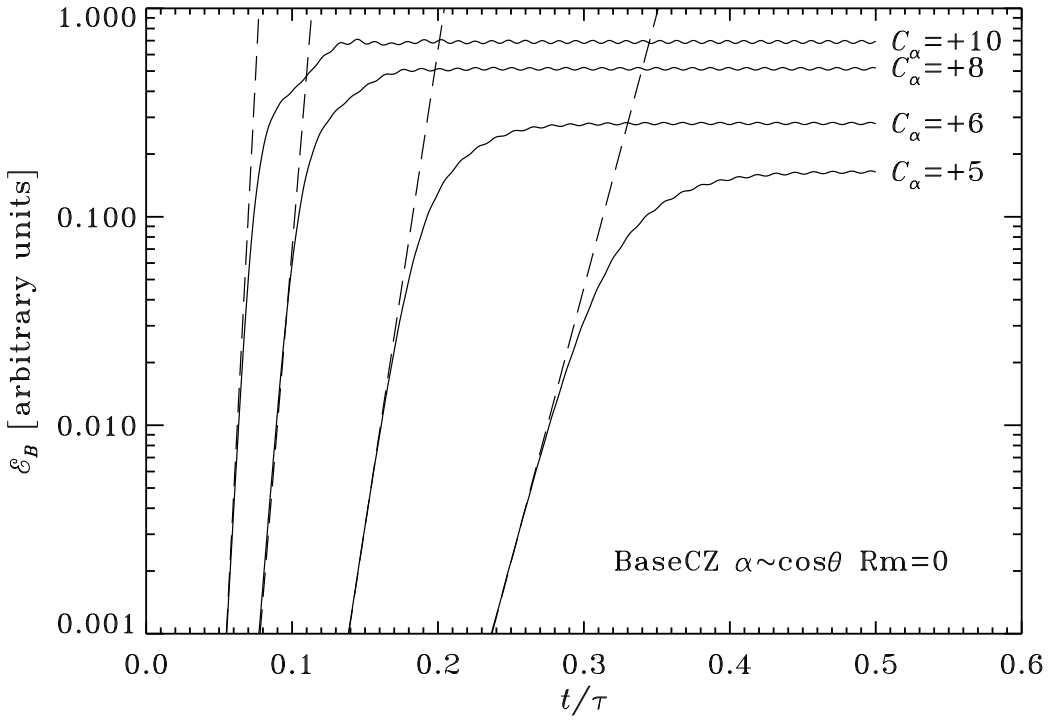

Figure 10.5: Time series of magnetic energy for a set of $\alpha\Omega$ dynamo solutions using our minimal $\alpha\Omega$ model including algebraic α-quenching, and different values for C_α, as labeled. Magnetic energy is expressed in arbitrary units. The dashed line indicates the exponential growth phase characterizing the linear regime.

10.2.4 Kinematic $\alpha\Omega$ models with α-quenching

With algebraic α-effect included in the poloidal source term, the mean-field $\alpha\Omega$ equations are now nonlinear, and are best solved as an initial-boundary-value problem. The initial condition is an arbitrary seed field of very low amplitude, in the sense that $B \ll B_{\rm eq}$ everywhere in the domain. Boundary conditions remain the same as for the linear analysis of the preceding section.

Consider again the minimal $\alpha\Omega$ model of §10.2.2, where the α-effect assumes its simplest possible latitudinal dependency, $\propto \cos\theta$. We use again $C_\Omega = 2.5\times10^4$, so that with $C_\alpha = +10$ this places the corresponding linear solution in the supercritical regime (see Figure 10.3). With a very weak **B** as initial condition, early on the model is essentially linear and exponential growth is expected. This is indeed what is observed, as can be seen on Fig. 10.5A, showing time series of the total magnetic energy in the simulation domain for increasing values of C_α, all above criticality. Eventually however, B starts to become comparable to $B_{\rm eq}$ in the region where the α-effect operates, leading to a break in exponential growth, and eventual saturation at some constant value of magnetic energy. Evidently, α-quenching is doing what it was designed to do! Note how the saturation energy level increases with increasing C_α, an intuitively satisfying behavior since solutions with larger C_α have a more powerful poloidal source term. The cycle frequency for these solutions is plotted as diamonds on Fig. 10.3B and, unlike in the linear solutions, now shows very little increase with increasing C_α. Moreover, the dynamo frequency of these α-quenched solutions are found to be slightly *smaller* that the frequency of the linear critical mode (here by some 10—15%), a behavior that is typical of mean-field dynamo models. Yet the overall form of the dynamo solutions closely resembles that of the linear eigenfunctions

plotted on Fig. 10.4. Indeed, the full cycle period is here $P/\tau \simeq 0.027$, which translates into 9 yr for our adopted $\eta_T = 5 \times 10^7\,\mathrm{m^2\ s^{-1}}$, i.e., a little over a factor of two shorter than the real thing. Not bad!

As a solar cycle model, these dynamo solutions do suffer from one obvious problem: magnetic activity is concentrated at too high latitudes (see Fig. 10.4). This is a direct consequence of the assumed $\cos\theta$ dependency for the α-effect. One obvious way to push the dynamo mode towards the equator is to (artificially) concentrate the α-effect at low latitude. By choosing in this manner an α-effect that "does the right thing", we are throwing away a significant chunk of whatever predictive capability our model might have had. The sad truth is that *ad hoc* specification of the α-effect is a long accepted practice in mean-field dynamo modeling (which of course does not make it any less *ad hoc*!). We therefore proceed nonetheless, using now a latitudinal dependency in $\propto \sin^2\cos\theta$ for the α-effect.

Figure 10.6 shows a selection of three $\alpha\Omega$ dynamo solutions, in the form of time-latitude diagrams of the toroidal field extracted at the core-envelope interface, here $r_c/R_\odot = 0.7$. If sunspot-producing toroidal flux ropes form in regions of peak toroidal field strength, and if those ropes rise radially to the surface, then such diagrams are directly comparable to the sunspot butterfly diagram of Fig 6.7. As before all models have $C_\Omega = 25000$, $|C_\alpha| = 10$, $\Delta\eta = 0.1$, and $\eta_T = 5 \times 10^7\,\mathrm{m^2\ s^{-1}}$. To facilitate comparison between solutions, antisymmetric parity was *imposed* via the boundary condition at the equator[9]. On such diagrams, the latitudinal propagation of dynamo waves shows up as a "tilt" of the flux contours away from the vertical direction.

The first solution, on Figure 10.6A, is once again our basic solution of Fig. 10.4, with an α-effect varying in $\cos\theta$. The other two use an α-effect varying in $\sin^2\cos\theta$, and so manage to produce dynamo action that materializes in two more or less distinct branches, one associated with the negative radial shear in the high latitude part of the tachocline, the other with the positive shear in the low-latitude tachocline. These two branches propagate in opposite directions, again in agreement with the Parker-Yoshimura sign rule, since the α-effect here does not change sign within an hemisphere.

It is noteworthy that co-existing dynamo branches, as on Fig. 10.6B and C, can have distinct dynamo periods, which in nonlinearly saturated solutions leads to long-term amplitude modulation. Such modulations are typically not expected in dynamo models where the only nonlinearity present is a simple algebraic quenching formula such as eq. (10.31). Note that this does not occur for the $C_\alpha < 0$ solution, where both branches propagate away from each other, but share a common latitude of origin and so are phased-locked at the onset (cf. Fig. 10.6B). We are seeing here a first example of potentially distinct dynamo modes interfering with one another, a direct consequence of the complex profile of solar internal differential rotation.

The solution of Fig. 10.6B is characterized by a low-latitude equatorially propagating branch, and a full cycle period of 16 yr, which is getting pretty close to the "target" 22yr. But again the strong high-latitude, poleward-propagating branch has no counterpart in the sunspot butterfly diagram. Well, no-problemo, we just concentrate the α-effect even more towards the equator, why not like $\propto \sin^4\theta\cos\theta$, say? It works, but I hope you are starting to find this general approach to the problem as silly as I do... let's try something else instead.

10.2.5 $\alpha\Omega$ models with meridional circulation

Meridional circulation can bodily transport the dynamo-generated magnetic field (terms labeled "advective transport" in eqs. (10.1)–(10.2)), and therefore, for a (presumably) solar-like equatorward return flow that is vigorous enough —in the sense of R_m being large enough— can presumably overpower the Parker-Yoshimura propagation rule embodied in eq. (10.30) and produce equatorward propagation no matter what the sign of the α-effect is. This is readily demonstrated in simple $\alpha\Omega$ models using a purely radial shear at the core-envelope interface (see references in bibliography), but with a solar-like differential rotation profile the situation turns out to be far more complex.

[9] Animations of the evolving solutions in meridional quadrant can be viewed on the course Web Page.

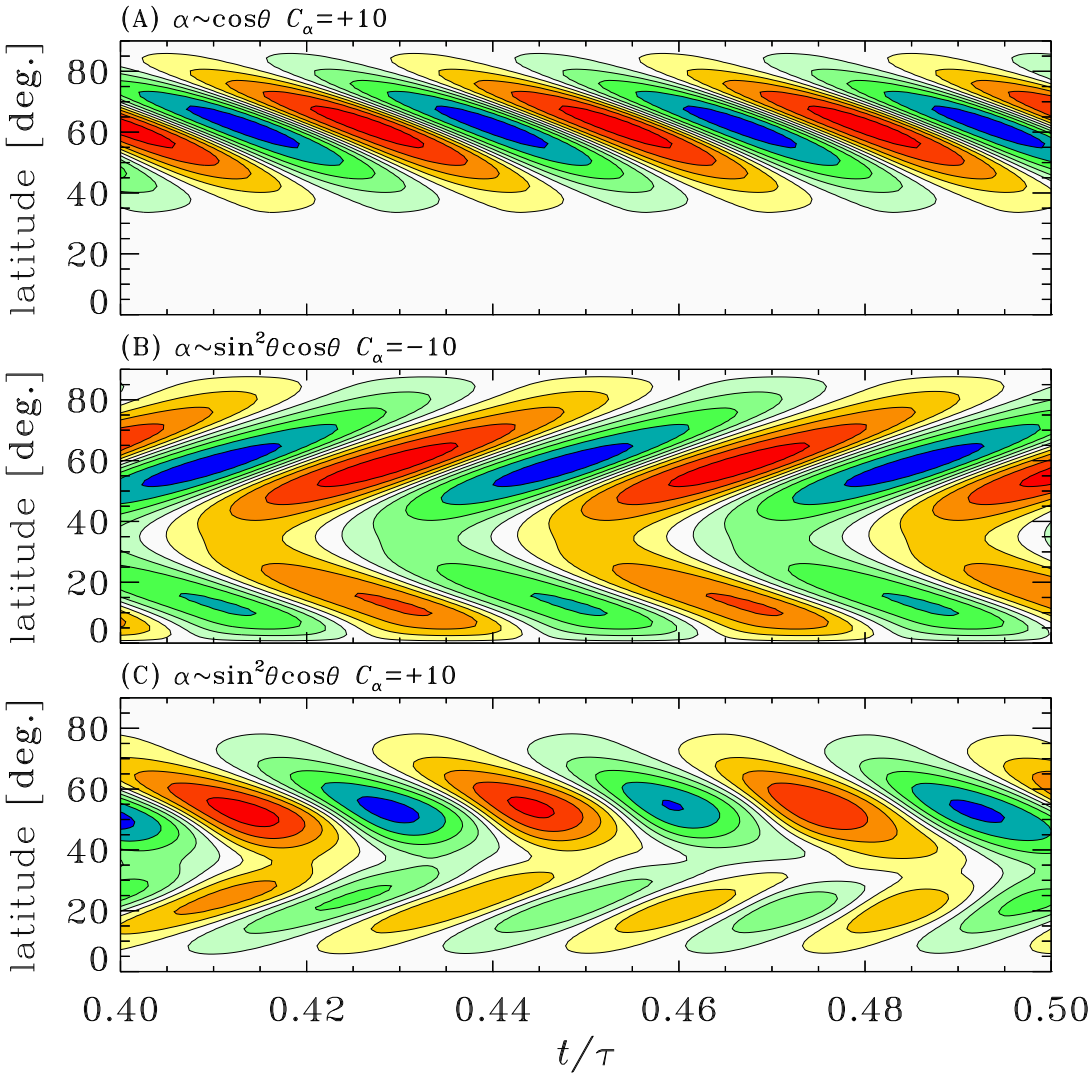

Figure 10.6: Northern hemisphere time-latitude ("butterfly") diagrams for a selection of nonlinear $\alpha\Omega$ dynamo solutions including α-quenching, constructed at the depth $r/R_\odot = 0.7$ corresponding to the core-envelope interface. Isocontours of toroidal field are normalized to their peak amplitudes, and plotted for increments $\Delta B/\max(B) = 0.2$, with yellow-to-red (green-to-blue) contours corresponding to $B > 0$ (< 0). The assumed latitudinal dependence of the α-effect is on given each panel. Other model ingredients as on Fig. 10.1. Note the co-existence of two distinct cycles in the solution shown on panel C, with periods differing by about 25%, which translates in a modulation of the magnetic energy timeseries.

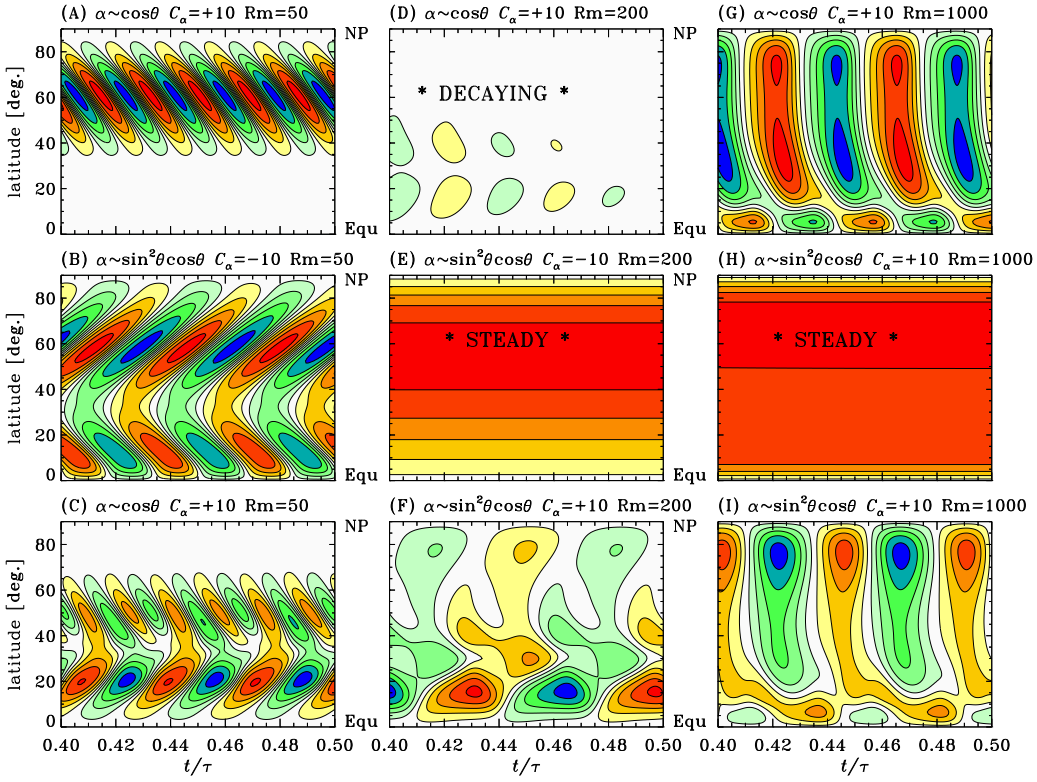

Figure 10.7: Time-latitude diagrams for the three $\alpha\Omega$ solutions depicted on Fig. 10.6, with meridional circulation now included; the solutions have $R_m = 50$ (left column), $R_m = 200$ (middle column), and $R_m = 10^3$ (left column). For the turbulent diffusivity value adopted here, $\eta_T = 5 \times 10^7$ m^2 s^{-1}, $R_m = 200$ corresponds to a solar-like circulation speed.

Starting from our three $\alpha\Omega$ dynamo solutions of Fig. 10.6, new solutions are now recomputed, this time including meridional circulation. Results are shown on Fig. 10.7, for three increasing values of the circulation flow speed, as measured by R_m. At $R_m = 50$, little difference is seen with the circulation-free solutions, except for the $C_\alpha = +10$ solution with $\alpha \propto \sin^2\theta\cos\theta$, (Fig. 10.7C), where the equatorial branch is now dominant and the polar branch has shifted to mid-latitudes and is cyclic with twice the frequency of the equatorial branch. At $R_m = 200$, correponding here to a solar-like circulation speed, drastic changes have materialized in all solutions. The negative C_α solution has now transited to a steady dynamo mode, that in fact persists to higher R_m values (panels E and H). The $C_\alpha = +10$ solution with $\alpha \propto \cos\theta$ is decaying at $R_m = 200$, while the solution with equatorially-concentrated α-effect starts to show a hint of equatorward propagation at mid-latitudes (panel F). At $R_m = 10^3$, the circulation has overwhelmed the dynamo wave, and both positive C_α solutions show equatorially-propagating toroidal fields (panels G and I).

Evidently, meridional circulation can have a profound influence on the overall character of the solutions. The behavioral turnover from dynamo wave-like solutions to circulation-dominated magnetic field transport sets in when the circulation speed becomes comparable to the propagation speed of the dynamo wave. In the circulation-dominated regime, the cycle period loses sensitivity to the assumed turbulent diffusivity value, and becomes determined primarily by the circulation's turnover time. This can be seen on Fig. 10.7: at $R_m = 50$ the solutions on panels (A) and (C) have markedly distinct (primary) cycle periods, while at $R_m = 10^3$ (panels G and I) the cycle periods are nearly identical. Note however that significant

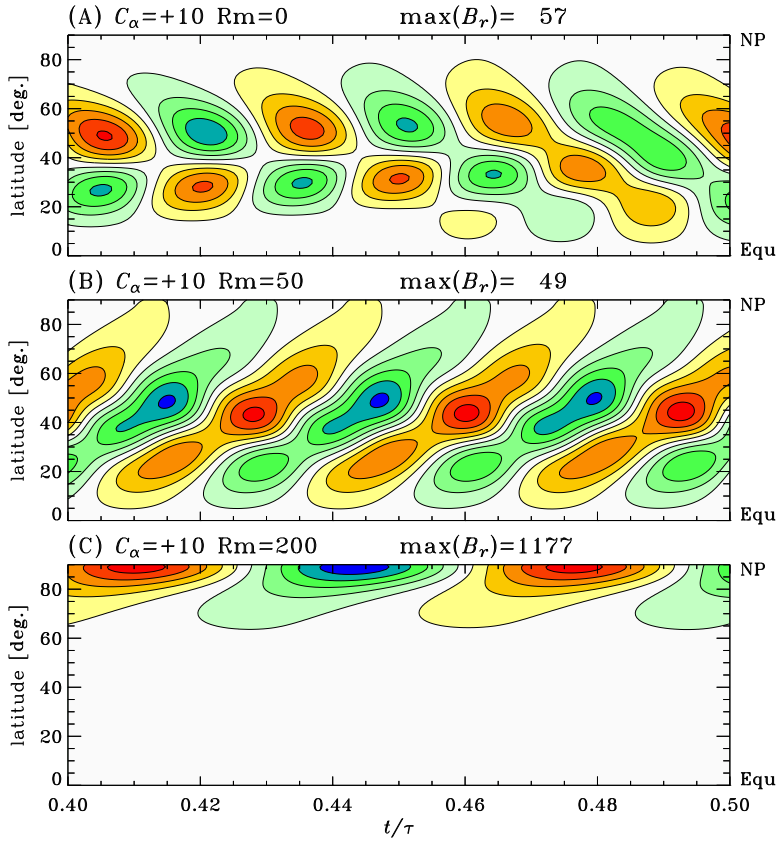

Figure 10.8: Time-latitude diagrams of the surface radial magnetic field, for increasing values of the circulation speed, as measured by the Reynolds number R_m. This is an $\alpha\Omega$ solution with the α-effect concentrated at low-latitude (see §10.2 and Fig. 10.6B). Recall that the $\mathrm{R}_m = 0$ solution on panel A exhibits amplitude modulation (cf. Figs. 10.6C).

effects require a large R_m ($\gtrsim 10^3$ for the circulation profile used here), which, u_0 being fixed by surface observations, translates into a magnetic diffusivity $\eta_T \lesssim 10^7 \mathrm{m}^2\mathrm{s}^{-1}$; by most orders-of-magnitude estimates constructed in the framework of mean-field electrodynamics, this is rather low.

Meridional circulation can also dominate the spatiotemporal evolution of the radial surface magnetic field, as shown on Figure 10.8 for a sequence of solutions with $\mathrm{R}_m = 0$, 50, and 200 (corresponding toroidal butterfly diagram at the core-envelope interface are plotted on Figs. 10.6C and 10.7C, F). In the circulation-free solution ($\mathrm{R}_m = 0$), the equatorward drift of the surface radial field is a direct reflection of the equatorward drift of the deep-seated toroidal field (see Fig. 10.6B). With circulation turned on, however, the surface magnetic field is swept instead towards the pole (Fig. 10.8B), becoming strongly concentrated and amplified there for solar-like circulation speeds ($\mathrm{R}_m = 200$, Fig. 10.8C) as a consequence of magnetic flux conservation in a converging flow. This concentrated poloidal field, when advected downwards to the polar regions of the tachocline, is responsible for the strong polar branch often seen in the butterfly diagram of dynamo solutions including a rapid meridional circulation (see, e.g., Fig. 10.7I).

10.2.6 Interface dynamos

The α-quenching expression (eq. (10.31)) used in the two preceding sections amounts to saying that dynamo action saturates once the mean, dynamo-generated field reaches an energy density comparable to that of the driving turbulent fluid motions, i.e., $B_{\rm eq} \sim \sqrt{\mu_0 \rho} v$, where v is the turbulent velocity amplitude. This appears eminently sensible, since from that point on a toroidal fieldline would have sufficient tension to resist deformation by cyclonic turbulence, and so could no longer feed the α-effect. At the base of the solar convective envelope, one finds $B_{\rm eq} \sim 0.1\,{\rm T}$, for $v \sim 10\,{\rm m\ s^{-1}}$, according to standard mixing length theory of convection. However, various calculations and numerical simulations have indicated that long before the mean toroidal field B reaches this strength, the helical turbulence reaches equipartition with the *small-scale*, turbulent component of the magnetic field. Such calculations also indicate that the ratio between the small-scale and mean magnetic components should itself scale as ${\rm R}_m^{1/2}$, where ${\rm R}_m = v\ell/\eta$ is a magnetic Reynolds number based on the turbulent speed but *microscopic* magnetic diffusivity. This then leads to the alternate quenching expression

$$\alpha \rightarrow \alpha(B) = \frac{\alpha_0}{1 + {\rm R}_m (B/B_{\rm eq})^2} \ . \tag{10.32}$$

known in the literature as *strong α-quenching* or *catastrophic quenching*. Since ${\rm R}_m \sim 10^8$ in the solar convection zone, this leads to quenching of the α-effect for very low amplitudes ofr the mean magnetic field, of order $10^{-5}\,{\rm T}$. Even though significant field amplification is likely in the formation of a toroidal flux rope from the dynamo-generated magnetic field, we are now a very long way from the 1—10 T demanded by simulations of buoyantly rising flux ropes and sunspot formation (see §6.2.3).

A way out of this difficulty was proposed by E.N. Parker under in the form of **interface dynamos**. The idea is beautifully simple: if the toroidal field quenches the α-effect, amplify and store the toroidal field away from where the α-effect is operating! Parker showed that in a situation where a radial shear and α-effect are segregated on either side of a discontinuity in magnetic diffusivity taken to coincide with the core-envelope interface, the constant coefficient $\alpha\Omega$ dynamo equations considered already in §9.3 support solutions in the form of travelling surface waves localized on the discontinuity in diffusivity. The key aspect of Parker's (linear, cartesian, analytical) solution is that for supercritical dynamo waves, the ratio of peak toroidal field strength on either side of the discontinuity surface is found to scale with the diffusivity ratio as

$$\frac{\max(B_2)}{\max(B_1)} \sim \left(\frac{\eta_2}{\eta_1} \right)^{-1/2} \ , \tag{10.33}$$

where the subscript "1" refers to the low-η region below the core-envelope interface, and "2" to the high-η region above. If one assumes that the envelope diffusivity (η_2) is of turbulent origin then $\eta_2 \sim \ell v$, so that the toroidal field strength ratio then scales as $\sim (v\ell/\eta_1)^{1/2} \equiv {\rm R}_m^{1/2}$. This is precisely the factor needed to bypass strong α-quenching.

As an example, Figure 10.9A shows a butterfly diagram for a numerical interface solution with $C_\Omega = 2.5 \times 10^5$, $C_\alpha = +10$, and a core-to-envelope diffusivity contrast $\Delta\eta = 10^{-2}$. The differential rotation and magnetic diffusivity profiles are the same as before, but here the α-effect is now (even more artificially) concentrated towards the equator, by imposing a latitudinal dependency $\alpha \sim \sin(4\theta)$ for $\pi/4 \leq \theta \leq 3\pi/4$, and zero otherwise. The poleward propagating equatorial branch is precisely what one would expect from the combination of positive radial shear and positive α-effect according to the Parker-Yoshimura sign rule[10].

The model does achieve the kind of toroidal field amplification one would like to see in interface dynamos. This can be seen on Figure 10.9B, which shows radial cuts of the toroidal field taken at latitude $\pi/8$, and spanning half a cycle. Notice how the toroidal field peaks below

[10]Note however that for this particular choice of α, η and Ω profiles, solutions with negative C_α are non-oscillatory in most of the $[C_\alpha, C_\Omega, \Delta\eta]$ parameter space.

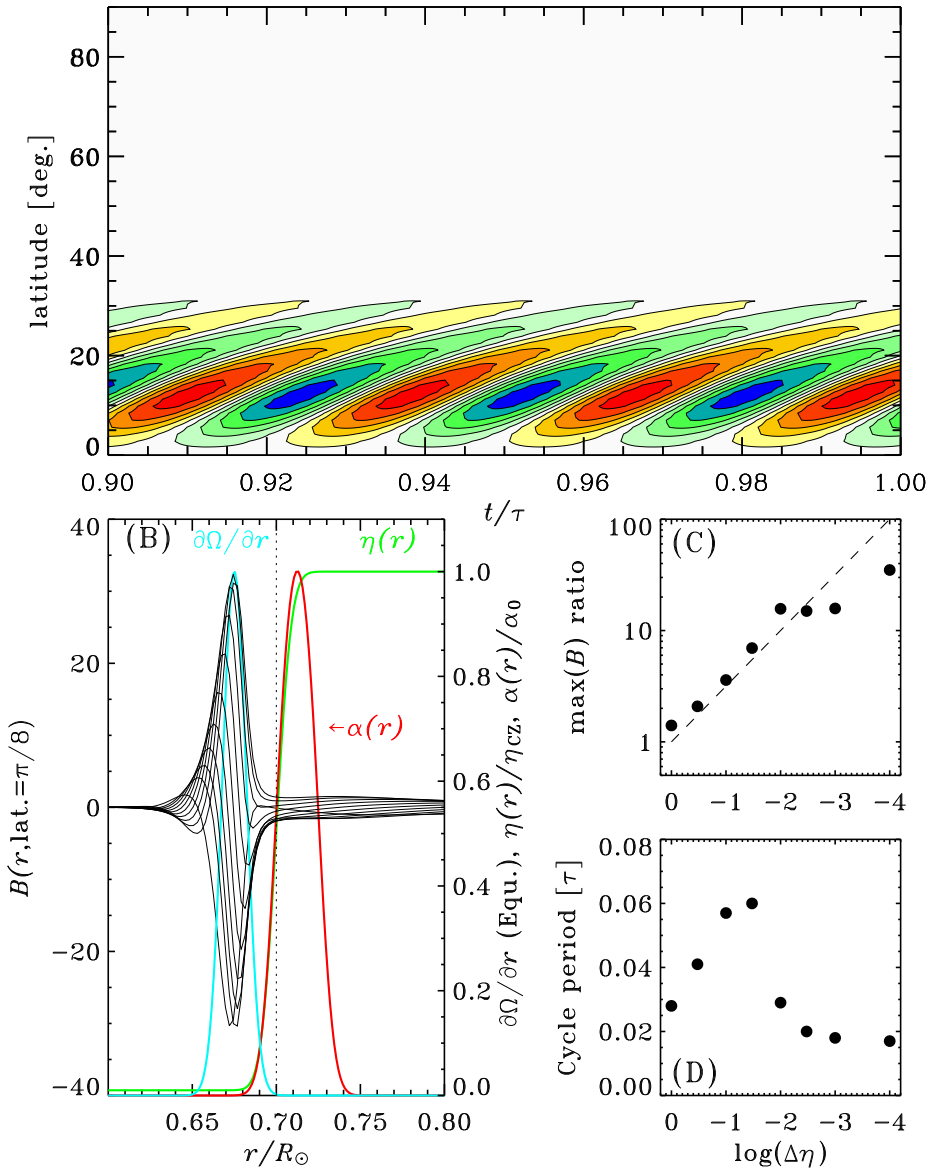

Figure 10.9: A representative interface dynamo model in spherical geometry. This solution has $C_\Omega = 2.5 \times 10^5$, $C_\alpha = +10$, and a core-to-envelope diffusivity contrast of 10^{-2}. Panel (A) shows a sunspot butterfly diagram, and panel B a series of radial cuts of the toroidal field at latitude 15^o. The (normalized) radial profiles of magnetic diffusivity, α-effect, and radial shear are also shown, again at latitude 15^o. The core-envelope interface is again at $r/R_\odot = 0.7$ (dotted line), where the magnetic diffusivity varies near-discontinuously. Panels (C) and (D) show the variations of the core-to-envelope peak toroidal field strength and dynamo period with the diffusivity contrast, for a sequence of otherwise identical dynamo solutions.

the core-envelope interface (vertical dotted line), well below the α-effect region and near the peak in radial shear. Figure 10.9C shows how the ratio of peak toroidal field below and above r_c varies with the imposed diffusivity contrast $\Delta\eta$. The dashed line is the dependency expected from eq. (10.33). For relatively low diffusivity contrast, $-1.5 \leq \log(\Delta\eta) \lesssim 0$, both the toroidal field ratio and dynamo period increase as $\sim (\Delta\eta)^{-1/2}$. Below $\log(\Delta\eta) \sim -1.5$, the $\max(B)$-ratio increases more slowly, and the cycle period falls. This is basically an electromagnetic skin-depth effect; unlike in the original picture proposed by Parker, here the poloidal field must diffuse down a finite distance into the tachocline before shearing into a toroidal component can commence. With this distance set by our adopted profile of $\Omega(r,\theta)$, as $\Delta\eta$ becomes very small there comes a point where the dynamo period is such that the poloidal field cannot diffuse as deep as the peak in radial shear in the course of a half cycle. The dynamo then runs on a weaker shear, thus yielding a smaller field strength ratio and weaker overall cycle.

10.3 Babcock-Leighton models

Solar cycle models based on what is now called the Babcock-Leighton mechanism were first developed in the early 1960's, yet they were temporarily eclipsed by the rise of mean-field electrodynamics a few years later. Their revival was motivated in part by the fact that synoptic magnetographic monitoring over solar cycles 21 and 22 has offered strong evidence that the surface polar field reversals are indeed triggered by the decay of active regions (see Fig. 6.12). The crucial question is whether this is a mere side-effect of dynamo action taking place independently somewhere in the solar interior, or a dominant contribution to the dynamo process itself.

Figure 10.10 illustrates the basic idea of the Babcock-Leighton mechanism. Consider the two bipolar magnetic regions (BMR) sketched on part (A). Recall that each of these is the photospheric manifestation of a toroidal flux rope emerging as an Ω-loop. The *leading* (*trailing*) component of each BMR is that located ahead (behind) in the direction of the Sun's rotation (from E to W). Joy's Law (§6.2.2) states that, on average, the leading component is located at lower latitude than the trailing component, so that a line joining each component of the pair makes an angle with respect to the E-W line. Hale's polarity law also inform us that the leading/trailing magnetic polarity pattern is opposite in each hemisphere, a reflection of the equatorial antisymmetry of the underlying toroidal flux system.

Horace W. Babcock demonstrated empirically from his observation of the sun's surface solar magnetic field that as the BMRs decay (presumably under the influence of turbulent convection), the trailing components drift to higher latitudes, leaving the leading components at lower latitudes, as sketched on Fig. 10.10B. Babcock also argued that the trailing polarity poloidal flux released to high latitude by the cumulative effects of the emergence and subsequent decay of many BMRs was responsible for the reversal of the sun's large-scale dipolar field. More germane from the dynamo point of view, the Babcock-Leighton mechanism taps into the (formerly) toroidal flux in the BMR to produce a poloidal magnetic component. To the degree that a positive dipole moment is being produced from a toroidal field that is positive in the N-hemisphere, this is a bit like a positive α-effect in mean-field theory. In both cases the Coriolis force is the agent imparting a twist on a magnetic field; with the α-effect this process occurs on the small spatial scales and operates on individual magnetic fieldlines. In contrast, the Babcock-Leighton mechanism operates on the large scales, the twist being imparted via the the Coriolis force acting on the flow generated along the axis of a buoyantly rising magnetic flux tube.

10.3.1 Sunspot decay and the Babcock-Leighton mechanism

Evidently this mechanism can operate as sketched on Figure 10.10 provided the magnetic flux in the leading and trailing components of each (decaying) BMR are separated in latitude faster than they can diffusively cancel with one another. Moreover, the leading components must end up at low enough latitudes for diffusive cancellation to take place across the equator. This

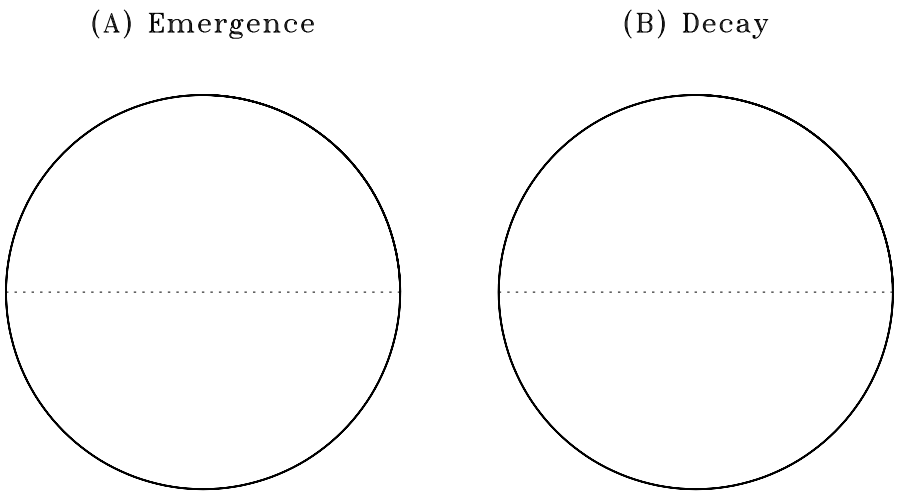

Figure 10.10: Cartoon of the Babcock-Leighton mechanism. On the left, two bipolar magnetic regions (BMR) have emerged, one in each hemisphere, with opposite leading/following polarity patterns, as per Hale's polarity Law. After some time the BMRs have decayed, the leading components have reconnected across the equator, while the trailing components have moved to higher latitudes. The net effect is the buildup of an hemispheric flux of opposite polarity in the N and S hemisphere, i.e., a net dipole moment (see text).

is not trivial to achieve, and we now take a more quantitative looks at the Babcock-Leighton mechanism, first with a simple 2D numerical model.

The starting point of the model is the grand sweeping assumption that, once the sunspots making up the bipolar active region lose their cohesiveness, their subsequent evolution can be approximated by the passive advection and resistive decay of the radial magnetic field component. This drastic simplification does away with any dynamical effect associated with magnetic tension and pressure within the spots, as well as any anchoring with the underlying toroidal flux system. The model is further simplified by treating the evolution of B_r as a two-dimensional transport problem on a spherical surface corresponding to the solar photosphere. Consequently, no subduction of the radial field can take place.

Even under these simplifying assumptions, the evolution is still governed by the MHD induction equation, specifically its r-component. The imposed flow is made of an axisymmetric "meridional circulation" and differential rotation:

$$\mathbf{u}(\theta) = 2u_0 \sin\theta\cos\theta\hat{\mathbf{e}}_\theta + \Omega_S(\theta) R \sin\theta \hat{\mathbf{e}}_\phi \ , \tag{10.34}$$

where Ω_S is the surface differential rotation profile used in the preceeding chapter (see eq. (10.9)). Note that $\nabla \cdot \mathbf{u} \neq 0$, a direct consequence of working on a spherical surface without possibility of subduction. Introducing a new latitudinal variable $\mu = \cos\theta$ and neglecting all radial derivatives, the r-component of the induction equation (evaluated at $r = R$) becomes:

$$\frac{\partial B_r}{\partial t} = \frac{2u_0}{R}(1-\mu^2)\left[B_r + \mu\frac{\partial B_r}{\partial \mu}\right] - \Omega_S(1-\mu^2)^{1/2}\frac{\partial B_r}{\partial \phi}$$

$$+\frac{\partial}{\partial \mu}\left[\frac{\eta}{R^2}\frac{\partial B_r}{\partial \mu}\right] + \frac{\partial}{\partial \phi}\left[\frac{\eta}{R^2(1-\mu^2)}\frac{\partial B_r}{\partial \phi}\right] \ , \tag{10.35}$$

with η being the magnetic diffusivity. As usual, we work with the nondimensional form of eq. (10.35), obtained by expressing time in units of $\tau_c = R/u_0$, i.e., the advection time associated

with the meridional flow. This leads to the appearance of the following two nondimensional numbers in the scaled version of eq. (10.35):

$$\mathrm{R}_m = \frac{u_0 R}{\eta} \ , \qquad \mathrm{R}_u = \frac{u_0}{\Omega_0 R} \ . \tag{10.36}$$

Using $\Omega_0 = 3 \times 10^{-6}\,\mathrm{rad\ s^{-1}}$, $u_0 = 15\,\mathrm{m\,s^{-1}}$, and $\eta = 6 \times 10^8\,\mathrm{m^2 s^{-1}}$ yields $\tau_\mathrm{c} \simeq 1.5\,\mathrm{yr}$, $\mathrm{R}_m \simeq 20$ and $\mathrm{R}_u \simeq 10^{-2}$. The former is really a measure of the (turbulent) magnetic diffusivity, and is the only free parameter of the model, as R_u is well constrained by surface Doppler measurements. The corresponding magnetic diffusion time is $\tau_\eta = R^2/\eta \simeq 26\,\mathrm{yr}$, so that $\tau_\mathrm{c}/\tau_\eta \ll 1$.

Figure 10.11 shows a representative solution. The initial condition (panel A, $t = 0$) mimics a series of eight BMRs, four per hemisphere, equally spaced 90^o apart at latitudes $\pm 45°$. Each BMR consists of two Gaussian profiles of opposite sign and adding up to zero net flux, with angular separation $d = 10°$ and with a line joining the center of the two Gaussians tilted with respect to the E-W direction[11] by an angle γ, itself related to the latitude θ_0 of the BMR's midpoint according to the Joy's Law-like relation:

$$\sin\gamma = 0.5 \cos\theta_0 \ . \tag{10.37}$$

The symmetry of the initial condition means that the problem can be solved in a single hemisphere with $B_r = 0$ enforced in the equatorial plane, in a 90° wide longitudinal wedge with periodic boundary conditions in ϕ.

The combined effect of circulation, diffusion and differential rotation is to concentrate the magnetic polarity of the trailing "spot" to high latitude, while the polarity of the leading spot remains near the original location of the active region. This is readily seen upon calculating the longitudinally averaged latitudinal profiles of B_r, as shown on Fig. 10.11F for the five successive epochs shown on (A)—(E). The poleward displacement of the trailing polarity "bump" is the equivalent to Babcock's original cartoon (cf. 10.10). The time required to achieve this here is $t/\tau_\mathrm{c} \sim 1$, and scales[12] as $(\mathrm{R}_m/\mathrm{R}_u)^{1/3}$.

We can use these simulation results to estimate the "efficiency" of the Babcock-Leighton mechanism. First we define the mean signed and unsigned magnetic flux:

$$\Phi = \mid \langle B_r \rangle \mid \ , \qquad F = \langle \mid B_r \mid \rangle \ , \tag{10.38}$$

where the averaging operator on the spherical surface is simply

$$\langle B_r \rangle = -\int_0^{2\pi} \int_{-1}^{+1} B_r \mathrm{d}\mu \mathrm{d}\phi \ . \tag{10.39}$$

Figure 10.12 shows the time-evolution of the signed (Φ, solid line) and unsigned (F, dashed) fluxes for the solution of Fig. 10.11. The unsigned flux decreases rapidly at first, then settles into a slower decay phase[13]. Meanwhile a small but significant hemispheric signed flux is building up. This is a direct consequence of (negative) flux cancellation across the equator, mediated by diffusion, and is the Babcock-Leighton mechanism in action. Note the dual, conflicting role of diffusion here; it is needed for cross-hemispheric flux cancellation, yet must be small enough to allow the survival of a significant trailing polarity flux on timescales of order τ_c.

The efficiency (Ξ) of the Babcock-Leighton mechanism, i.e., converting toroidal to poloidal field, can be defined as the ratio of the signed flux at $t = \tau_\mathrm{c}$ to the BMR's initial unsigned flux[14]:

$$\Xi = 2\frac{\Phi(t = \tau_\mathrm{c})}{F(t = 0)} \ . \tag{10.40}$$

[11] Remember that this is meant to represent the result of a toroidal flux rope erupting through the surface, so that in this case the underlying toroidal field is positive, which is the polarity the polarity of the trailing "spot", as measured with respect to the direction of rotation, from left to right here.

[12] Can you figure that one out?

[13] This should remind you of something encountered a few chapter ago...

[14] Can you figure out why a factor of two was inserted on the RHS of eq. (10.40)?

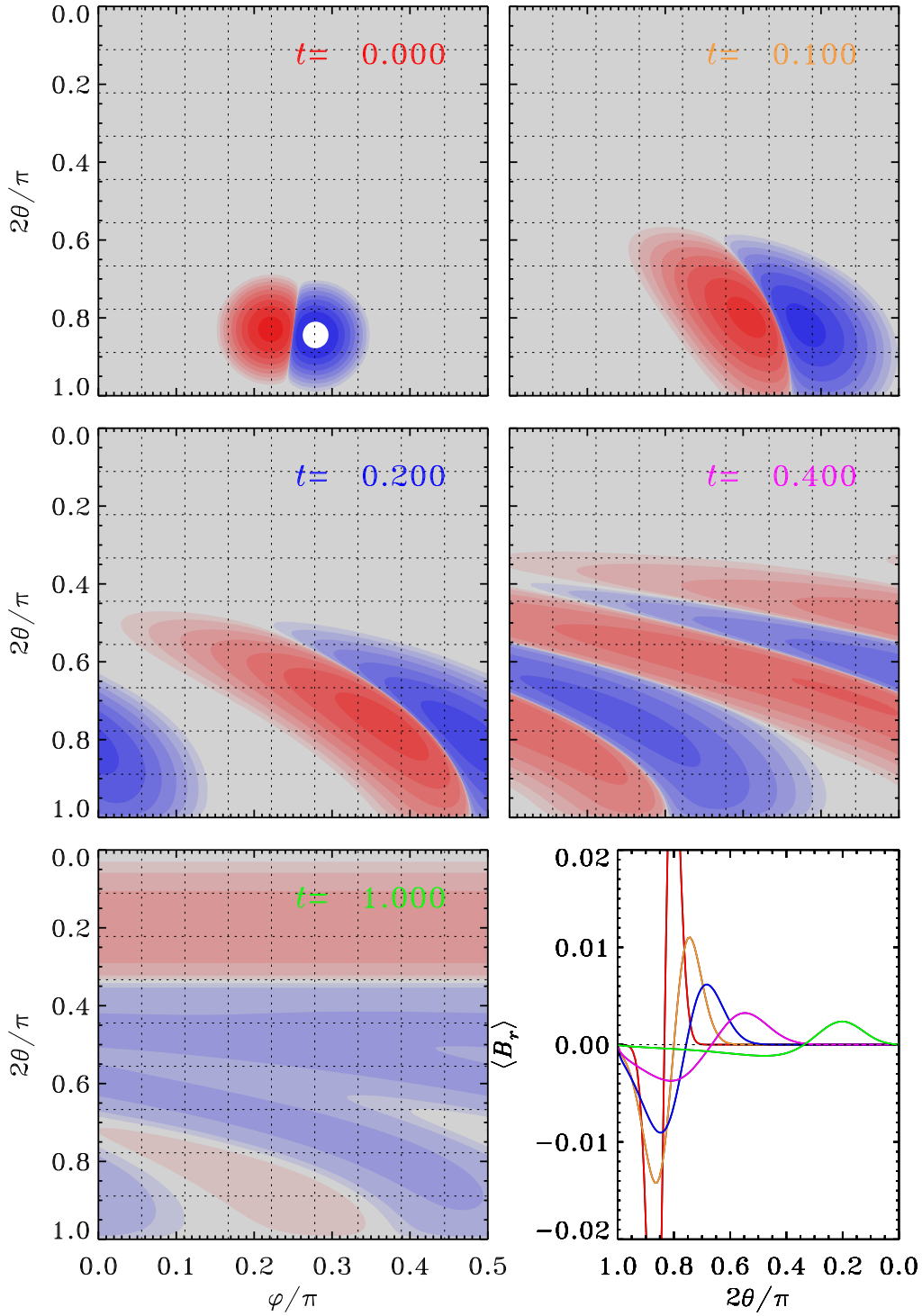

Figure 10.11: Evolution of the surface radial magnetic field component of a BMR located at 15 degrees latitude, as described by the 2D advection-diffusion equation (10.35). Parameter values are $\mathrm{R}_u = 10^{-2}$ and $\mathrm{R}_m = 50$, with time given in units of $\tau_c = R/u_0$. The bottom right panel shows the evolution of the longitudinally averaged radial magnetic field.

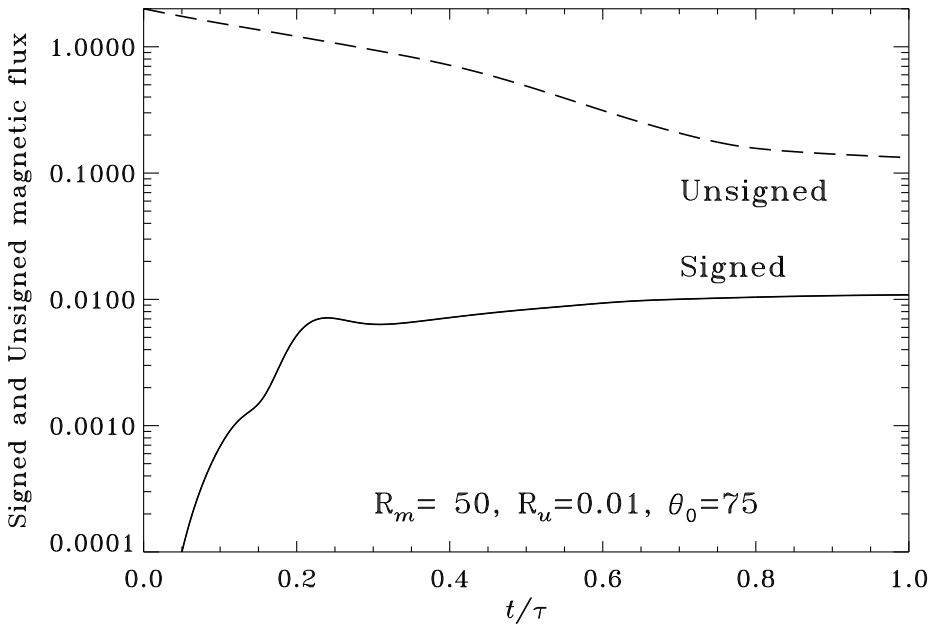

Figure 10.12: Evolution of the signed (solid line) and unsigned (dashed line) magnetic flux for BMRs emerging at latitudes 15 degrees.

Note that Ξ is independent of the assumed initial field strength of the BMRs since eq. (10.35) is linear in B_r. Looking back at Fig. 10.12, one would eyeball the efficiency at about 1% in converting the BMR flux to polar cap signed flux. This conversion efficiency turns out to be a rather complex function of BMR parameters; it is expected to increases with increasing tilt γ, and therefore should increasing with latitudes as per Joy's Law, yet proximity to the equator favors transequatorial diffusive flux cancellation of the leading component; moreover, having $\mathrm{d}u_\theta/\mathrm{d}\theta < 0$ favors the separation of the two BMR components, thus minimizing diffusive flux cancellation between the leading and trailing components.

10.3.2 Axisymmetrization revisited

Take another look at Fig. 10.11; at $t = 0$ (panel A) the surface magnetic field distribution is highly non-axisymmetric. By $t/\tau_c = 1$ (panel E), however, the field distribution shows a far less pronounced ϕ-dependency, especially at high latitudes where in fact B_r is nearly axisymmetric. This should remind you of something we encountered earlier: axisymmetrization of a non-axisymmetric magnetic field by an axisymmetric differential rotation (§7.3.5), the spherical analog of flux expulsion. In fact a closer look at the behavior of the unsigned flux on Fig. 10.12A (dashed line) already shows a hint of the two-timescale behavior we have come to expect of axisymmetrization: the rapid destruction of the non-axisymmetric flux component and slower ($\sim \tau_\eta$) diffusive decay of the remaining axisymmetric flux distribution.

Since the spherical harmonics represent a complete and nicely orthonormal functional basis on the sphere, it follows that the initial condition for the simulation of Fig. 10.11 can be written as

$$B_r^0(\theta,\phi) = \sum_{l=0}^{\infty} \sum_{m=-l}^{+l} b_{lm} Y_{lm}(\theta,\phi) \ , \tag{10.41}$$

where the Y_{lm}'s are the spherical harmonics:[15]

$$Y_{lm}(\theta,\phi) = \sqrt{\frac{2l+1}{4\pi}\frac{(l-m)!}{(l+m)!}} P_l^m(cos\theta) e^{im\phi} \ , \tag{10.42}$$

and with the coefficients b_{lm} given by

$$b_{lm} = \int_0^{2\pi} \int_0^{\pi} B_r^0(r,\theta) Y_{lm}^*(\theta,\phi) \ , \tag{10.43}$$

where the "$*$" indicates complex conjugation[16]. Now, axisymmetrization will wipe all $m \neq 0$ modes, leaving only the $m = 0$ modes to decay away on the slower diffusive timescale[17]. Therefore, at the end of the axisymmetrization process, the radial field distribution now has the form:

$$B_r(\theta) = \sum_{l=0}^{\infty} \sqrt{\frac{2l+1}{4\pi}} b_{l0} P_l(\cos\theta) \ , \qquad t/\tau_c \gg \mathrm{R}_u \ . \tag{10.44}$$

which now describes an axisymmetric poloidal magnetic field[18]

10.3.3 Dynamo models based on the Babcock-Leighton mechanism

So now we understand how the Babcock-Leighton mechanism can provide a poloidal source term in eq. (10.1). Now we need to construct a solar cycle model. One big difference with the $\alpha\Omega$ models considered in §10.2 is that the two source regions are now spatially segregated: production of the toroidal field takes place in the tachocline, as before, but now production of the poloidal field takes place in the surface layers.

The mode of operation of a generic solar cycle model based on the Babcock-Leighton mechanism is illustrated in cartoon form on Figure 10.13. Let P_n represent the amplitude of the high-latitude, surface ("A") poloidal magnetic field in the late phases of cycle n, i.e., after the polar field has reversed. The poloidal field P_n is advected downward by meridional circulation (A→B), where it then starts to be sheared by the differential rotation while being also advected equatorward (B→C). This leads to the growth of a new low-latitude (C) toroidal flux system, T_{n+1}, which becomes buoyantly unstable (C→D) and starts producing sunspots (D), which subsequently decay and release the poloidal flux P_{n+1} associated with the new cycle $n+1$. Poleward advection and accumulation of this new flux at high latitudes (D→A) then obliterates the old poloidal flux P_n, and the above sequence of steps begins anew. Meridional circulation clearly plays a key role in this "conveyor belt" model of the solar cycle, by providing the needed link between the two spatially segregated source regions.

10.3.4 The Babcock-Leighton poloidal source term

The definition of the Babcock-Leighton source term S to be inserted in eq. (10.1) is evidently the crux of the model. Consider the following:

$$S(r,\theta,B(t)) = s_0 f(r) \sin\theta\cos\theta \left[1 - \left(\frac{B(r_c,\theta,t)}{B_0}\right)^2\right]^{-1} B(r_c,\theta,t) \ , \tag{10.45}$$

with

$$f(r) = \frac{1}{2}\left[1 + \mathrm{erf}\left(\frac{r-r_2}{d_2}\right)\right]\left[1 - \mathrm{erf}\left(\frac{r-r_3}{d_3}\right)\right] \ , \tag{10.46}$$

[15] Better rewrite those factorials differently when trying a numerical implementation...

[16] What are the non-zero b_{lm} for the inclined dipole treated in §7.3.5?

[17] With $\mathbf{u} = 0$, the decay rate of those remaining modes are given by the eigenvalues of the 2D pure resistive decay problem, much like in §7.1.

[18] How would you go about computing the toroidal-to-poloidal efficiency factor Ξ within this modeling framework?

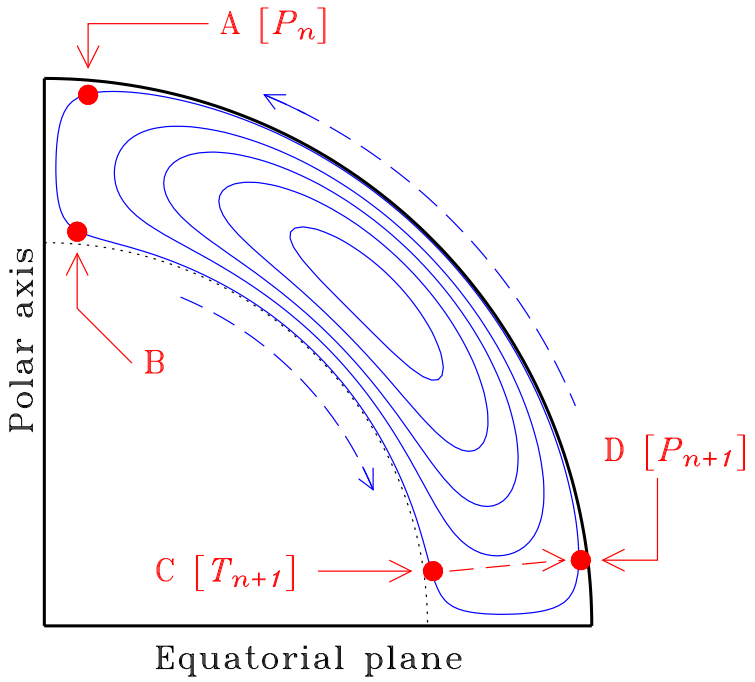

Figure 10.13: Operation of a solar cycle model based on the Babcock-Leighton mechanism. The diagram is drawn in a meridional quadrant of the sun, with streamlines of meridional circulation plotted in blue. Poloidal field having accumulated in the surface polar regions ("A") at cycle n must first be advected down to the core-envelope interface (dotted line) before production of the toroidal field for cycle $n+1$ can take place (B→C). Buoyant rise of flux rope to the surface (C→D) is a process taking place on a much shorter timescale.

where s_0 is a numerical coefficient setting the strength of the source term (corresponding dynamo number being $C_S = s_0 R/\eta_0$), and with the various remaining numerical coefficient taking the values $r_2/R = 0.95$, $r_3/R = 1$, $d_2 = d_3 = 10^{-2}R$, and $B_0 = 10\,\mathrm{T}$. Note that the dependency on B is *non-local*, i.e., it involves the toroidal field evaluated at the core-envelope interface r_c, (but at the same polar angle θ). The combination of error functions concentrate the source term immediately beneath the surface, which is fine. The nonlocality in B represents the fact that the strength of the source term is proportional to the field strength in the bipolar active region, itself presumably reflecting the strength of the diffuse toroidal field near the core-envelope interface, where the magnetic flux ropes eventually giving rise to the bipolar active region originate. The nonlocal quenching nonlinearity reflects the fact that as the strength of the flux rope reaches about 10 T, the flux rope emerges without the tilt essential to the Babcock-Leighton mechanism. The $\cos\theta$ dependency is a first order description of Joy's Law, i.e., the tilt of active regions increases with latitude. Notably missing in eq. (10.45) is some sort of lower threshold on S, to mimic the fact that flux ropes with field strengths lower than a few tens of teslas either fail to be destabilized in a short enough timescale, rise to the surface at high latitudes and without systematic tilt patterns, and/or fail altogether to survive their rise through the convective envelope.

At any rate, inserting this source term into eq. (10.1) is what we need to bypass Cowling's theorem and produce a viable dynamo model. The nonlocality of S notwithstanding, at this point the model equations are definitely mean-field like. Yet no averaging on small scales is involved. What is implicit in eq. (10.45) is some sort of averaging process at least in longitude

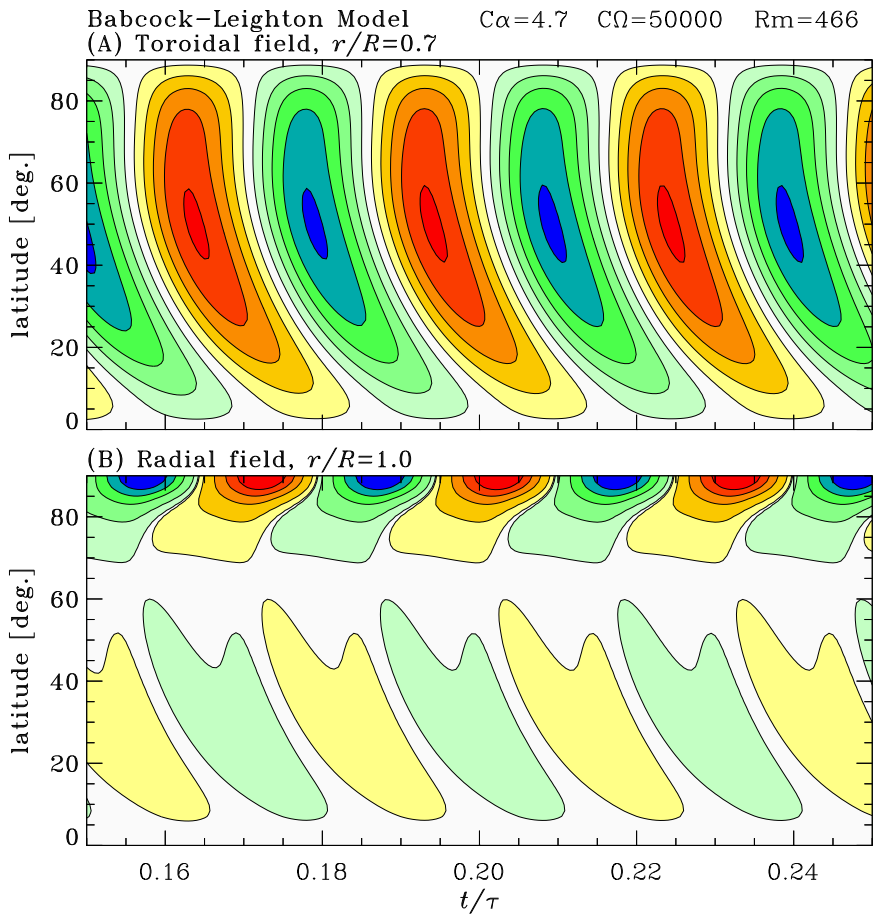

Figure 10.14: Time-latitude diagrams of the surface toroidal field at the core-envelope interface (panel A), and radial component of the surface magnetic field (panel B) in a Babcock-Leighton model of the solar cycle. This solution is computed for solar-like differential rotation and meridional circulation, the latter here closing at the core-envelope interface. The core-to-envelope contrast in magnetic diffusivity is $\Delta\eta = 1/300$, the envelope diffusivity $\eta_T = 2.5 \times 10^7\,\mathrm{m}^2\,\mathrm{s}^{-1}$, and the (poleward) mid-latitude surface meridional flow speed is $u_0 = 16\,\mathrm{m\,s}^{-1}$.

and time.

10.3.5 A sample solution

Figure 10.14 shows N-hemisphere time-latitude diagrams for the toroidal magnetic field at the core-envelope interface (panel A), and the surface radial field (panel B), for a representative Babcock-Leighton dynamo solutions computed following the model implementation described above. The equatorward advection of the toroidal field by meridional circulation is here clearly apparent, as well as the concentration of the surface radial field near the pole. Note how the polar radial field changes from negative (blue) to positive (red) at just about the time of peak positive toroidal field at the core-envelope interface; this is the phase relationship inferred from synoptic magnetograms (e.g., Fig. 6.12 herein) as well as observations of polar faculae

Although it exhibits the desired equatorward propagation, the toroidal field butterfly diagram on Fig. 10.14A peaks at much higher latitude ($\sim 45°$) than the sunspot butterfly diagram ($\sim 15°$–$20°$, cf. Fig. 6.7). This occurs because this is a solution with high magnetic diffusivity contrast, where meridional circulation closes at the core-envelope interface, so that the *latitudi-*

nal component of differential rotation dominates the production of the toroidal field. This difficulty can be alleviated by letting the meridional circulation penetrate below the core-envelope interface, but this often leads to the production of a strong polar branches, again a consequence of both the strong radial shear present in the high-latitude portion of the tachocline, and of the concentration of the poloidal field taking place in the high latitude-surface layer prior to this field being advected down into the tachocline by meridional circulation (viz. Figs. 10.13 and 10.14)

A noteworthy property of this class of model is the dependency of the cycle period on model parameters; over a wide portion of parameter space, the meridional flow speed is found to be the primary determinant of the cycle period (P). This behavior arises because, in these models, the two source regions are spatially segregated, and the time required for circulation to carry the poloidal field generated at the surface down to the tachocline is what effectively sets the cycle period. The corresponding time delay introduced in the dynamo process has rich dynamical consequences, to be discussed in §10.5 below. On the other hand, P is found to depend very weakly on the assumed values of the source term amplitude s_0, and turbulent diffusivity η_T; the latter is is very much unlike the behavior typically found in mean-field models, where P scales nearly as η_T^{-1} in α-quenched $\alpha\Omega$ mean-field models[19].

10.4 Models based on HD and MHD instabilities

In the presence of stratification and rotation, a number of hydrodynamical (HD) and magnetohydrodynamical (MHD) instabilities associated with the presence of a strong toroidal field in the stably stratified, radiative portion of the tachocline can lead to the growth of disturbances with a net helicity, which under suitable circumstances can produce a toroidal electromotive force, and therefore act as a source of poloidal field. Different types of solar cycle models have been constructed in this manner, the two most promising ones being briefly reviewed in this section. In both cases the resulting dynamo models end up being described by something closely resembling our now well-known axisymmetric mean-field dynamo equations, the novel poloidal field regeneration mechanisms being once again subsumed in an α-effect-like source term appearing of the RHS of eq. (10.1).

10.4.1 Models based on shear instabilities

Hydrodynamical stability analyses of the latitudinal shear profile in the solar tachocline indicate that the latter may be unstable to non-axisymmetric perturbations, with the instabilities planforms characterized by a net kinetic helicity, which, loosely inspired by eq. (9.56), allows the construction of an azimuthally-averaged α-effect-like source term that is directly proportional to the large-scale toroidal component, just as in mean-field electrodynamics.

Figure 10.15 shows representative time-latitude diagrams of the toroidal field at the core-envelope interface, and surface radial field. This is a solar-like solution with a mid-latitude surface meridional (poleward) flow speed of 17 m s^{-1}, envelope diffusivity $\eta_T = 5 \times 10^7\,m^2$ s^{-1}, a core-to-envelope magnetic diffusivity contrast $\Delta\eta = 10^{-3}$, and a simple α-quenching-like amplitude nonlinearity[20]. Note the equatorward migration of the deep toroidal field, set here by the meridional flow in the deep envelope, and the poleward migration and intensification of the surface poloidal field, again a direct consequence of advection by meridional circulation, as in the mean-field dynamo models discussed in §10.2.5) in the advection-dominated, high R_m regime. The three-lobe structure of each spatiotemporal cycle in the butterfly diagram reflects laittudinal structure in kinetic helicity profiles associated with the instability planforms.

The primary weakness of these models, in their present form, is their reliance on a linear stability analysis that altogether ignores the destabilizing effect of magnetic fields, especially

[19] OK hold it, how do you reconcile this statement with the near independence of the cycle period on C_α for the periods of α-quenched models plotted in Fig. 10.3B (dimonds)?

[20] See the Dikpati & Gilman (2001) paper cited in the bibliography for more details.

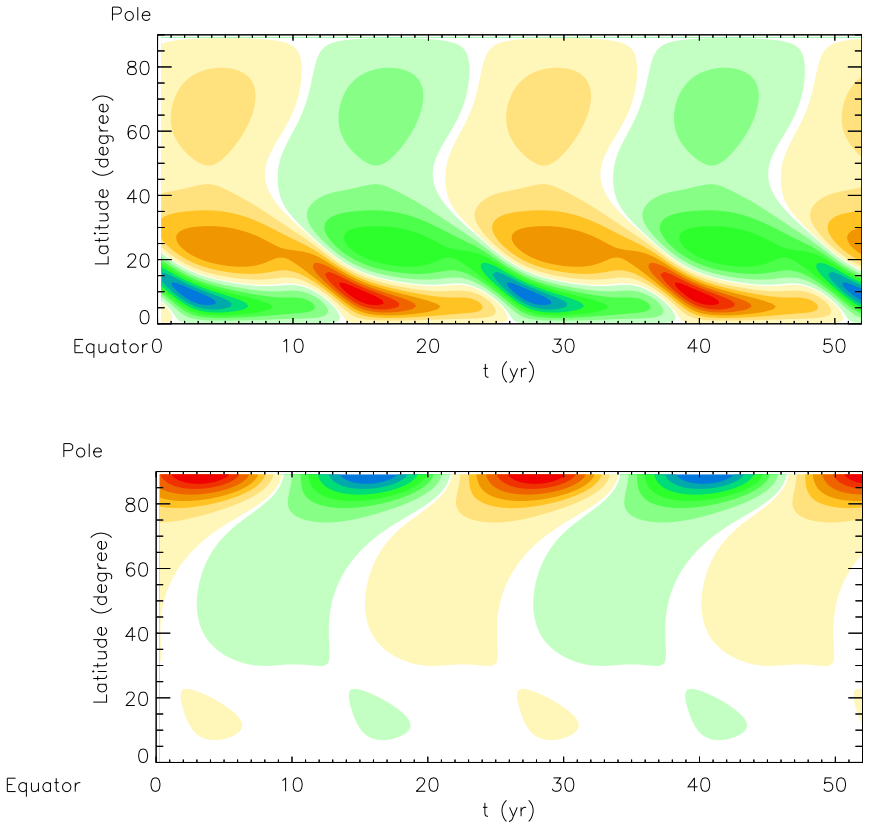

Figure 10.15: Time-latitude "butterfly" diagrams of the toroidal field at the core-envelope interface (left), and surface radial field (right) for a representative dynamo solution with the tachocline α-effect of Dikpati & Gilman. This solution has a solar-like half-period of eleven years. Note how the deep toroidal field peaks at very low latitudes, in good agreement with the sunspot butterfly diagram. For this solution the equatorial deep toroidal field and polar surface radial field lag each other by $\sim \pi$, but other parameter settings can bring this lag closer to the observed $\pi/2$. Diagrams kindly provided by M. Dikpati.

since MHD stability analyses have shown that the MHD version of the instability is easier to excite for toroidal field strengths of the magnitude believe to characterize the solar tachocline, Moreover, the planforms in the MHD version of the instability are highly dependent on the assumed underlying toroidal field profile, so that the kinetic helicity can be expected to (1) have a time-dependent latitudinal distribution, and (2) be intricately dependent on the mean toroidal field in a manner that is unlikely to be reproduced by a simple amplitude-limiting quenching formula.

10.4.2 Models based on flux tube instabilities

As briefly discussed in §6.2.3, modelling of the rise of thin toroidal flux tubes throughout the solar convection zone has met with great success, in particular in reproducing the latitudes of emergence and tilt angles of bipolar sunspot pairs. It is also possible to use the thin-flux tube approximation to study the stability of toroidal flux ropes stored immediately below the base of the convection zone, to investigate the conditions under which they can actually be destabilized and give rise to sunspots. Once the tube destabilizes, calculations show that under the influence of rotation, the correlation between the flow and field perturbations is such as to yield a mean azimuthal electromotive force, equivalent to a *positive* α-effect in the N-hemisphere.

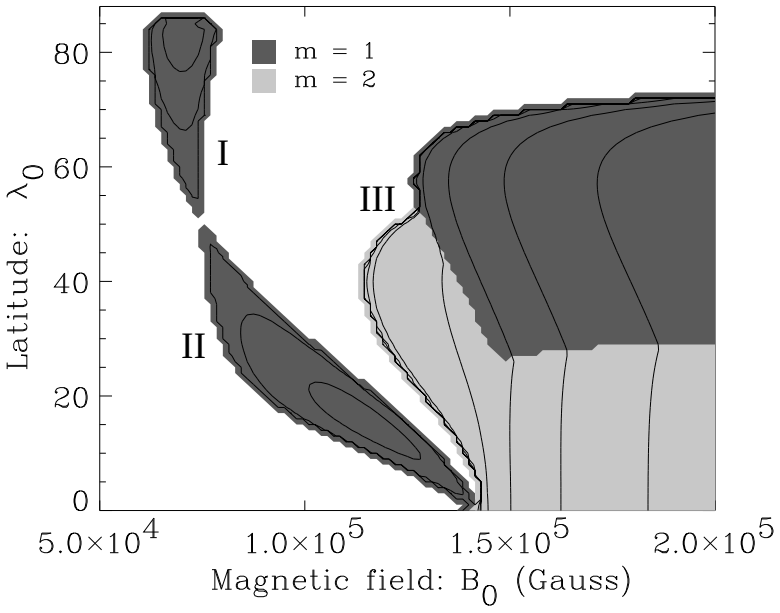

Figure 10.16: Stability diagram for toroidal magnetic flux tubes located in the overshoot layer immediately beneath the core-envelope interface. The plot shows contours of growth rates in the latitude-field strength plane. The gray scale encodes the azimuthal wavenumber of the mode with largest growth rate, and regions left in white are stable. Dynamo action is associated with the regions with growth rates $\sim 1\,\mathrm{yr}$, here labeled I and II. Diagram kindly provided by A. Ferriz-Mas.

Figure 10.16 shows a stability diagram for this flux tube instability, in the form of growth rate contours in a 2D parameter space comprised of flux tube strength and latitudinal position at the core-envelope interface. The key is now to identify regions where weak instability arises (growth rates $\gtrsim 1\,\mathrm{yr}$). In the case shown on Fig. 10.16, these regions are restricted to flux tube strengths in the approximate range 6—15 T.

Although it has not yet been comprehensively studied, this dynamo mechanism has a number of very attractive properties. It operates without difficulty in the strong field regime (in fact in *requires* strong fields to operate). It also naturally yields dynamo action concentrated at low latitudes. Difficulties include the need of a relatively finely tuned magnetic diffusivity to achieve a solar-like dynamo period, and a relatively finely-tuned level of subadiabaticity in the overshoot layer for the instability to kick on and off at the appropriate toroidal field strengths.

The effects of meridional circulation in this class of dynamo models has yet to be investigated; this should be particularly interesting, since both analytic calculations and numerical simulations suggest a *positive* α-effect in the Northern-hemisphere, which should then produce *poleward* propagation of the dynamo wave at low latitude. Meridional circulation could then perhaps produce equatorward propagation of the dynamo magnetic field even with a positive α-effect, as it does in true mean-field models (cf. §10.2.5).

As an interesting aside, note on Fig. 10.16 how flux tubes located at high latitudes are always stable; this is due to the stabilizing effect of magnetic tension associated with high curvature of the toroidal flux ropes. Even if flux ropes were to form there, they may not necessarily show up at the surface as sunspots. This should be kept in mind when comparing time-latitudes diagrams produced by this or that dynamo model to the sunspot butterfly diagram; the two may not map onto one another as well as often implicitly assumed.

10.5 Nonlinearities, fluctuations and intermittency

Given that the basic physical mechanism(s) underlying the operation of the solar cycle are not yet agreed upon, attempting to understand the origin of the observed *fluctuations* of the solar cycle may appear to be a futile undertaking. Nonetheless, work along these lines continues at full steam in part because of the high odds involved: the frequencies of all eruptive phenomena relevant to space weather are strongly modulated by the amplitude of the solar cycle; varying levels of solar activity may contribute significantly to climate change; and certain aspects of the observed fluctuations may actually hold important clues as to the physical nature of the dynamo process.

10.5.1 Cycle modulation through stochastic forcing

An obvious means of producing amplitude fluctuations in dynamo models is to introduce stochastic forcing in the governing equations. Sources of stochastic "noise" certainly abound in the solar interior; large-scale flows in the convective envelope, such as differential rotation and meridional circulation, are observed to fluctuate, an unavoidable consequence of dynamical forcing by the surrounding, vigorous turbulent flow. This convection is known to produce its own small-scale magnetic field (viz. Fig. 8.13), and amounts to a form of rapidly varying zero-mean "noise" superimposed on the slowly-evolving mean magnetic field. This can be readily incorporated into dynamo models by introducing, on the RHS of the governing equations, an additional zero-mean source term that varies randomly from node-to-node and from one time step to the next.

In addition, the azimuthal averaging implicit in all models of the solar cycle considered above will yield dynamo coefficients showing significant deviations about their mean values, as a consequence of the spatiotemporally discrete nature of the physical events (e.g., cyclonic updrafts, sunspot emergences, flux rope destabilizations, etc.) whose collective effects add up to produce a mean electromotive force. The impact of these statitical fluctuations about the mean can be modeled in a number of ways. Perhaps the most straightforward is to let the dynamo number fluctuate randomly in time about some pre-set mean value. By most statistical estimates, the expected magnitude of these fluctuations is quite large, i.e., many times the mean value, a conclusion is also supported by numerical simulations One typically also introduces a *coherence time* during which the dynamo number retains a fixed value. At the end of this time interval, this value is randomly readjusted. Depending on the dynamo model at hand, the coherence time can be related to the lifetime of convective eddies (α-effect-based mean-field models), to the decay time of sunspots (Babcock-Leighton models), or to the growth rate of instabilities (hydrodynamical shear or buoyant MHD instability-based models).

Figure 10.17 shows some representative results for three $\alpha\Omega$ dynamo solutions with fluctuation in the dynamo number C_α ranging from $\pm 50\%$ (blue) to $\pm 200\%$ (red). While the correlation time amounts here to only 5% of the half-cycle period, note on Fig. 10.17A how modulations on much longer timescales appear in the magnetic energy time series. As can be seen on Fig. 10.17B, the fluctuations also lead to a spread in the cycle period, although here little (anti)correlation is seen with the cycle's amplitude. Here both the mean cycle period and amplitude increase with increasing fluctuation amplitude.

In linear $\alpha\Omega$ near criticality, noise can introduce an anticorrelation between cycle amplitude and duration that is reminiscent of the Waldmaier Rule (Fig. 6.6). Unfortunately, this interesting result in general does not carry over to nonlinearly-saturated $\alpha\Omega$ dynamo solutions, although it has been noted in at least one Babcock-Leighton solar cycle model. See the bibliography for entry points into this vast literature.

10.5.2 Cycle modulation through the Lorentz force

The dynamo-generated magnetic field will, in general, produce a Lorentz force that will tend to oppose the driving fluid motions. This is a basic physical effect that should be included in any

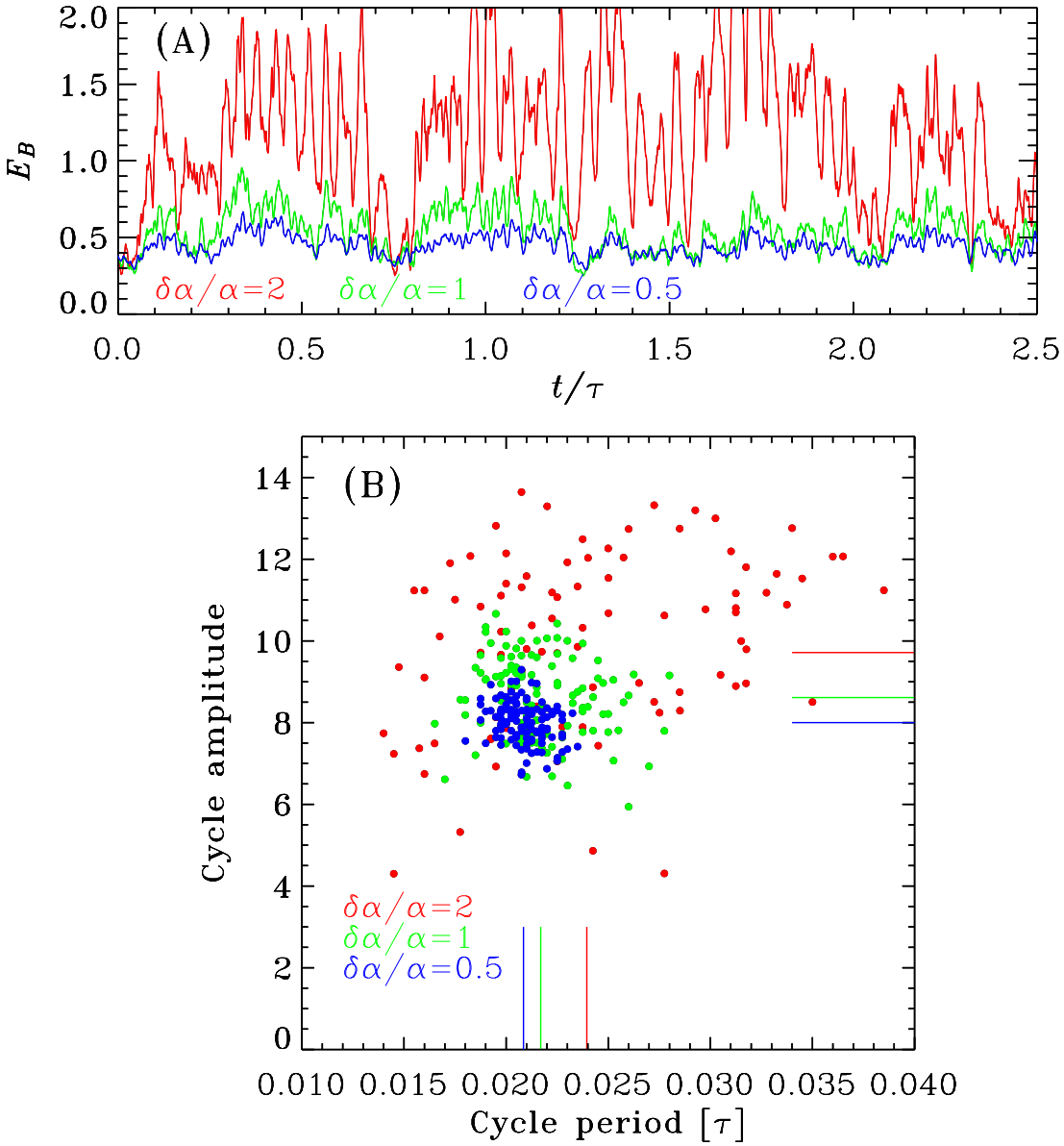

Figure 10.17: Stochastic fluctuations of the dynamo number in an $\alpha\Omega$ mean-field dynamo solution. The reference, unperturbed solution is the same as that plotted of Fig. 10.6D, except that is uses a lower value for the dynamo number, $C_\alpha = -5$. Panel (A) shows magnetic energy time series for three solutions with increasing fluctuation amplitudes, while panel (B) shows a correlation plot of cycle amplitude and duration, as extracted from a time series of the toroidal field at the core-envelope interface ($r/R = 0.7$) in the model. Solutions are color-coded according to the relative amplitude $\delta C_\alpha/C_\alpha$ of the fluctuations in the dynamo number. Line segments on panel (B) indicate the mean cycle amplitudes and durations for the three solutions. The correlation time of the noise amounts here to about 5% of the mean half-cycle period in all cases.

dynamo model. It is not all trivial to do so, however, since in a turbulent environment both the fluctuating and mean components of the magnetic field can affect both the large-scale flow components, as well as the small-scale turbulent flow providing the Reynolds stresses powering the large-scale flows. One must thus distinguish between two (related) amplitude-limiting mechanisms:

1. Lorentz force associated with the mean magnetic field *directly* affecting large-scale flow (sometimes called the "Malkus-Proctor effect");
2. Large-scale magnetic field *indirectly* affecting large-scale flow via effects on small-scale turbulence and associated Reynolds stresses (sometimes called "Λ-quenching")

Introducing magnetic backreaction on differential rotation and/or meridional circulation is a tricky business, because one must then also, in principle, provide a model for the Reynolds stresses powering the large-scale flows in the solar convective envelope as well as a procedure for computing magnetic backreaction on these. This rapidly leads into the unyielding realm of MHD turbulence, although algebraic "Λ-quenching" formulae akin to α-quenching have been proposed based on specific turbulence models. Alternately, one can add an *ad hoc* source term to the RHS of eq. (1.80), designed in such a way that in the absence of the magnetic field, the desired solar-like large-scale flow is obtained. As a variation on this theme, one can simply divide the large-scale flow into two components, the first ($\mathbf{U}$) corresponding to some prescribed, steady profile, and the second ($\mathbf{U}'$) to a time-dependent flow field driven by the Lorentz force

$$\mathbf{u} = \mathbf{U}(\mathbf{x}) + \mathbf{U}'(\mathbf{x}, t, \mathbf{B}) \ , \tag{10.47}$$

with the (non-dimensional) governing equation for $\mathbf{U}'$ including only the Lorentz force and a viscous dissipation term on its RHS. If $\mathbf{u}$ amounts only to differential rotation, then $\mathbf{U}'$ must obey a (nondimensional) differential equation of the form

$$\frac{\partial \mathbf{U}'}{\partial t} = \frac{\Lambda}{4\pi\rho}(\nabla \times \mathbf{B}) \times \mathbf{B} + \mathrm{P}_m \nabla^2 \mathbf{U}' \tag{10.48}$$

where time has been scaled according to the magnetic diffusion time $\tau = R_\odot^2/\eta_T$, as before. Two dimensionless parameters appear in eq. (10.48). The first (Λ) is a numerical parameter measuring the influence of the Lorentz force. The second, $\mathrm{P}_m = \nu/\eta$, is the *magnetic Prandtl number*. It measures the relative importance of viscous and Ohmic dissipation. When $\mathrm{P}_m \ll 1$, large velocity amplitudes in $\mathbf{U}'$ can be produced by the dynamo-generated mean magnetic field. This effectively introduces an additional, long timescale in the model, associated with the evolution of the magnetically-driven flow; the smaller P_m, the longer that timescale.

The majority of studies published thus far and using this approach have only considered the nonlinear magnetic backreaction on differential rotation. This has been shown to lead to a variety of behaviors, including amplitude and parity modulation, periodic or aperiodic, as well as intermittency (more on the latter in §10.5.4). It has been argued that amplitude modulation in such models can be divided into two main classes:

1. Type-I modulation corresponds to a nonlinear interaction between modes of different parity, with the Lorenz Force-mediated flow variations controlling the transition from one mode to another;
2. Type-II modulation refers to an exchange of energy between a single dynamo mode (of some fixed parity) with the flow field. This leads to quasiperiodic modulation of the basic cycle, with the modulation period controlled by the magnetic Prandtl number.

Both types of modulation can co-exists in a given dynamo model, leading to a rich overall dynamical behavior. Figure 10.18 shows two butterfly diagrams produced by a nonlinear mean-field interface model[21]. The model is defined on cartesian slab with a reference differential

[21] For details on this model see paper by Tobias (1997) cited in the bibliography.

rotation varying only with depth, and includes backreaction on the differential rotation according to the procedure described above. The model exhibits strong, quasi-periodic modulation of the basic cycle, leading to epochs of strongly reduced amplitude. Note how the dynamo can emerge from such epochs with strong hemispheric asymmetries (top panel), or with a different parity (bottom panel). It is not clear, at this writing, to what degree these behaviors are truly generic, as opposed to model-dependent.

The differential rotation can also be supressed indirectly by magnetic backreaction on the *small-scale* turbulent flow that produce the Reynolds stresses driving the large-scale mean flow. Inclusion of this so-called "Λ-quenching" in mean-field dynamo models, alone or in conjunction with other amplitude-limiting nonlinearities, has also been shown to lead to a variery of periodic and aperiodic amplitude modulations, provided the magnetic Prandtl number is small[22]. This type of models stand or fall with the turbulence model they use to compute the various mean-field coefficients, and it is not yet clear which aspects of the results are truly generic to Λ-quenching.

The dynamical backreaction of the large-scale magnetic field on meridional circulation has received comparatively little attention. The few calculations published so far[23] suggest that diffuse toroidal magnetic fields of strength up to 0.1 T can probably be advected equatorward at the core-envelope interface That it can indeed do so is crucial models relying on the meridional flow to produce equatorward propagation of magnetic fields as the cycle unfolds.

10.5.3 Cycle modulation through time delays

It was already noted that in solar cycle models based on the Babcock-Leighton mechanism of poloidal field generation, meridional circulation effectively sets —and even regulates— the cycle period. In doing so, it also introduces a long time delay in the dynamo mechanism, "long" in the sense of being comparable to the cycle period. This delay originates with the time required for circulation to advect the surface poloidal field down to the core-envelope interface, where the toroidal component is produced (A→C on Fig. 10.13). In contrast, the production of poloidal field from the deep-seated toroidal field (C→D), is a "fast" process, growth rates and buoyant rise times for sunspot-forming toroidal flux ropes being of the order of a few months. The first, long time delay turns out to have important dynamical consequences.

The long time delay inherent in B-L models of the solar cycle allows a formulation of cycle-to-cycle amplitude variations in terms of a simple one-dimensional iterative map. Working in the kinematic regime, neglecting resistive dissipation, and in view of the conveyor belt argument of §10.3, the toroidal field strength (T_{n+1}) at cycle $n+1$ is assumed to be linearly proportional to the poloidal field strength (P_n) of cycle n, i.e.,

$$T_{n+1} = aP_n \ . \tag{10.49}$$

Now, because flux eruption is a fast process, the strength of the poloidal field at cycle $n+1$ is (nonlinearly) proportional to the toroidal field strength of the *current* cycle:

$$P_{n+1} = f(T_{n+1})T_{n+1} \ . \tag{10.50}$$

Here the "Babcock-Leighton" function $f(T_{n+1})$ measures the efficiency of surface poloidal field production from the deep-seated toroidal field. Substitution of eq. (10.49) into eq. (10.50) leads immediately to a one-dimensional iterative map:

$$p_{n+1} = \alpha f(p_n)p_n \ , \tag{10.51}$$

where the p_n's are normalized amplitudes, and the normalization constants as well as the constant a in eq. (10.49) have been absorbed into the definition of the map's parameter α,

[22] See, e.g., the paper by Küker et al. (1999) cited in the bibliography.
[23] See papers by Rempel (2001, 2002) cited in the bibliography.

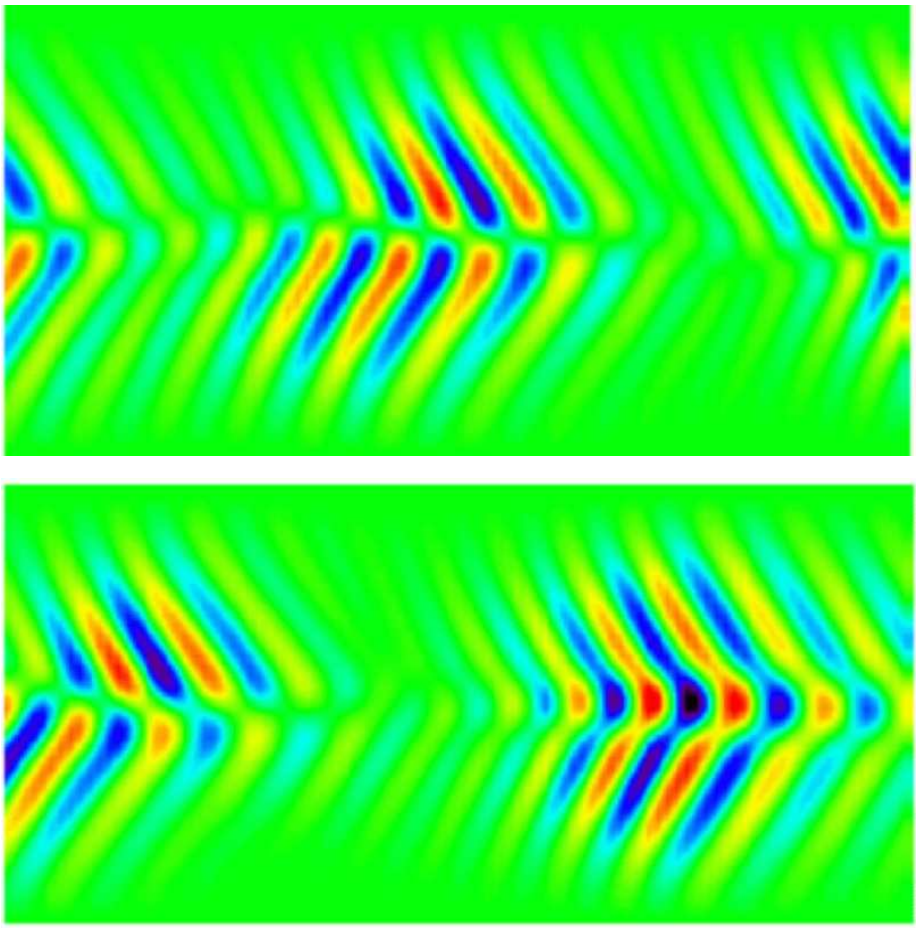

Figure 10.18: Amplitude and parity modulation in a dynamo model including magnetic backreaction on the differential rotation. These are the usual time-latitude diagrams for the toroidal magnetic field, now covering both solar hemispheres, and exemplify type I (bottom) and type II (top) modulation arising in nonlinear dynamo models with backreaction on the differential rotation (see text). Figure kindly provided by S.M. Tobias.

here operationally equivalent to a dynamo number. We consider here the following nonlinear function

$$f(p) = \frac{1}{4}\left[1 + \mathrm{erf}\left(\frac{p-p_1}{w_1}\right)\right]\left[1 - \mathrm{erf}\left(\frac{p-p_2}{w_2}\right)\right] \ , \tag{10.52}$$

with $p_1 = 0.6$, $w_1 = 0.2$, $p_2 = 1.0$, and $w_2 = 0.8$. This catches an essential feature of the B-L mechanism, namely the fact that it can only operate in a finite range of toroidal field strength.

A bifurcation diagram for the resulting iterative map is presented on Figure 10.19A. For a given value of the map parameter α, the diagram gives the locus of the amplitude iterate p_n for successive n values. The "critical dynamo number" above which dynamo action becomes possible, corresponds here to $\alpha = 0.851$ ($p_n = 0$ for smaller α values). For $0.851 \leq \alpha \leq 1.283$, the iterate is stable at some finite value of p_n, which increases gradually with α. This corresponds to a constant amplitude cycle. As α reaches 1.283, period doubling occurs, with the iterate p_n alternating between high and low values (e.g., $p_n = 0.93$ and $p_n = 1.41$ at $\alpha = 1.4$). Further period doubling occurs at $\alpha = 1.488$, then at $\alpha = 1.531$, then again at $\alpha = 1.541$, and ever faster until a point is reached beyond which the amplitude iterate seems to vary without any obvious pattern (although within a bounded range); this is in fact a chaotic regime.

As in any other dynamo model where the source regions for the poloidal and toroidal magnetic field components are spatially segregated, the type of time delay considered here is unavoidable. The B-L model is just a particularly clear-cut example of such a situation. One is then led to anticipate that the map's rich dynamical behavior should find its counterpart in the original, arguably more realistic spatially-extended, diffusive axisymmetric model that inspired the map formulation. Remarkably, this is indeed the case.

Fig. 10.19B shows a bifurcation diagram, conceptually equivalent to that shown on part A, but now constructed from a sequence of numerical solutions of the Babcock-Leighton model discussed earlier in §10.3, for increasing values of the dynamo number in a version of that model where the source term includes uses the combination of error functions as in eq. (10.52) to set the nonlinear (and still nonlocal) dependence of S on the toroidal field B. Time series of magnetic energy were calculated from the numerical solutions, and successive peaks found and plotted for each individual solution. The sequence of period doubling eventually leading to a chaotic regime, is strikingly similar to the bifurcation diagram constructed from the corresponding iterative map, down to the narrow multiperiodic windows interspersed in the chaotic domain. This demonstrates that time delay effects are a robust feature, and represent a very powerful source of cycle amplitude fluctuation in Babcock-Leighton models, even in the kinematic regime.

10.5.4 Intermittency

The term "intermittency" refers to systems undergoing apparently random, rapid switching from quiescent to bursting behaviors, as measured by the magnitude of some suitable system variable. In the context of solar cycle model, intermittency is invoked to explain the existence of Maunder Minimum-like quiescent epochs of strongly suppressed activity randomly interspersed within periods of "normal" cyclic activity[24].

Intermittency has been shown to occur through stochastic fluctuations of the dynamo number in mean-field dynamo models operating at or near criticality[25]. This mechanism for "on-off intermittency" works well, however there is no strong reason to believe that the solar dynamo is running just at criticality, so that is not clear how good an explanation this is of Maunder-type grand minima. Parity modulation driven by stochastic noise can also lead to a form of

[24]It should be noted, however, that dearth of sunspots does not necessarily means a halted cycle; as noted earlier, flux ropes of strengths inferior to ~ 1 T will not survive their rise through the convective envelope, and the process of flux rope formation from the dynamo-generated mean magnetic field may itself be subjected to a threshold in field strength. The same basic magnetic cycle may well have continued unabated all the way through the Maunder Minimum, but at an amplitude just below one of these thresholds. This idea finds support in the ^{10}Be radioisotope record, which shows a clear and uninterrupted cyclic signal through the Maunder minimum (see Fig. 6.8).

[25]see paper by Ossendrijver & Hoyng (1996) in the bibliography for a particularly lucid discussion.

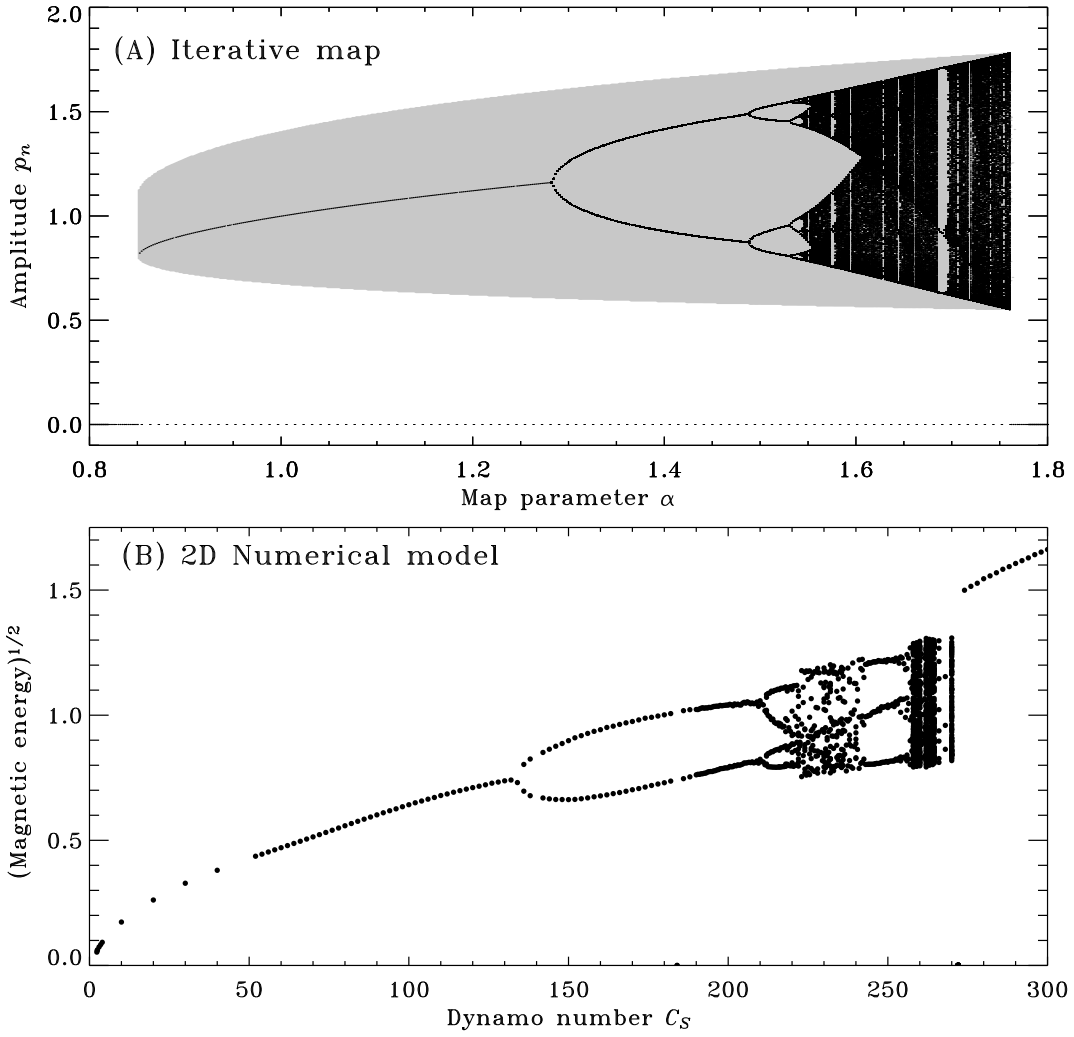

Figure 10.19: Two bifurcation diagrams for a kinematic Babcock-Leighton model, where amplitude fluctuations are produced by time-delay feedback. The top diagram is computed using the one-dimensional iterative map given by eqs. (10.51)–(10.52), while the bottom diagram is reconstructed from numerical solutions in spherical geometry, of the type discussed in §10.3. The shaded area in panel (A) maps the attraction basin for the cyclic solutions, with initial conditions located outside of this basin converging to the trivial solution $p_n = 0$.

intermittency, by exciting the higher-order modes that perturb the normal operation of the otherwise dominant dynamo mode, producing strongly reduced cycle amplitudes[26].

Another way to trigger intermittency in a dynamo model is to let nonlinear dynamical effects, for example a reduction of the differential rotation amplitude, push the effective dynamo number below its critical value; dynamo action then ceases during the subsequent time interval needed to reestablish differential rotation following the diffusive decay of the magnetic field; in the low P_m regime, this time interval can amount to many cycle periods, but P_m must not be too small, otherwise grand minima become too rare Values $\mathrm{P}_m \sim 10^{-2}$ seems to work best. Such intermittency is most readily produced when the dynamo is operating close to criticality[27].

Intermittency has also been observed in strongly supercritical model including α-quenching as the sole amplitude-limiting nonlinearity. Such solutions can enter grand minima-like epochs of reduced activity when the dynamo-generated magnetic field completely quenches the α-effect. The dynamo cycle restarts when the magnetic field resistively decays back to the level where the α-effect becomes operational once again. The physical origin of the "long" timescale governing the length of the "typical" time interval between successive grand minima episodes is unclear, and the physical underpinning of intermittency harder to identify[28].

Intermittency can also arise naturally in dynamo models characterized by a lower operating threshold on the magnetic field. These include models where the regeneration of the poloidal field takes place via the MHD instability of toroidal flux tubes (§10.4.2). In such models, the transition from quiescent to active phases requires an external mechanism to push the field strength back above threshold. This can be stochastic noise[29], or a secondary dynamo process normally overpowered by the "primary" dynamo during active phases. Figures 10.20 show one representative solution of the latter variety, where intermittency is driven by a weak α-effect-based kinematic dynamo operating in the convective envelope, in conjunction with magnetic flux injection into the underlying region of primary dynamo action by randomly positioned downflows[30]. The top panel shows a sample trace of the toroidal field, and the bottom panel a butterfly diagram constructed near the core-envelope interface in the model.

Dynamo models exhibiting amplitude modulation through time-delay effects are also liable to show intermittency in the presence of stochastic noise. This intermittency mechanism hinges on the fact that the map's attractor has a finite basin of attraction (indicated by gray shading on Fig. 10.19A). Stochastic noise acting simultaneously with the map's dynamics can then knock the solution out of this basin of attraction, which then leads to a collapse onto the trivial solution $p_n = 0$, even if the map parameter remains supercritical. Stochastic noise eventually knocks the solution back into the attractor's basin, which signals the onset of a new active phase. This behavior was indeed found in a Babcock-Leighton model similar to that described in §10.3 Figure 10.21 shows one such representative solution, in the same format as Fig. 10.20. This is a dynamo solution which, in the absence of noise, operates in the singly-periodic regime. Stochastic noise is added to the vector potential $A\hat{\mathbf{e}}_\phi$ in the surface layers, and the dynamo number is also allowed to fluctuate randomly about a pre-set mean value. The resulting solution exhibits both amplitude fluctuations and intermittency.

With its strong polar branch often characteristic of dynamo models with meridional circulation, Fig. 10.21 is not a particularly good fit to the solar butterfly diagram. Yet its fluctuating behavior is solar-like in a number of ways, including epochs of alternating higher-than-average and lower-than-average cycle amplitudes (the Gnevyshev-Ohl rule, cf. Fig. 6.6), and residual pseudo-cyclic variations during quiescent phases, as suggested by ^{10}Be data. This later property is due at least in part to meridional circulation, which continues to advect the (diffusively decaying) magnetic field after the dynamo has fallen below threshold.

[26]For more on this version of noise-driven intermittency mechanism, see the paper by Mininni & Gomez (2004) cited in the bibiography.

[27]See, e.g., the papers by Küker et al. (1999) and Brooke et al. (2002) cited in the bibliography.

[28]For representative models exhibiting intermittency of this type, see the paper by Tworkowski et al. (1998) cited in the bibliography.

[29]See the paper by Schmitt et al. (1996) cited in the bibliography.

[30]for more details see paper by Ossendrijver (2000) in bibliography

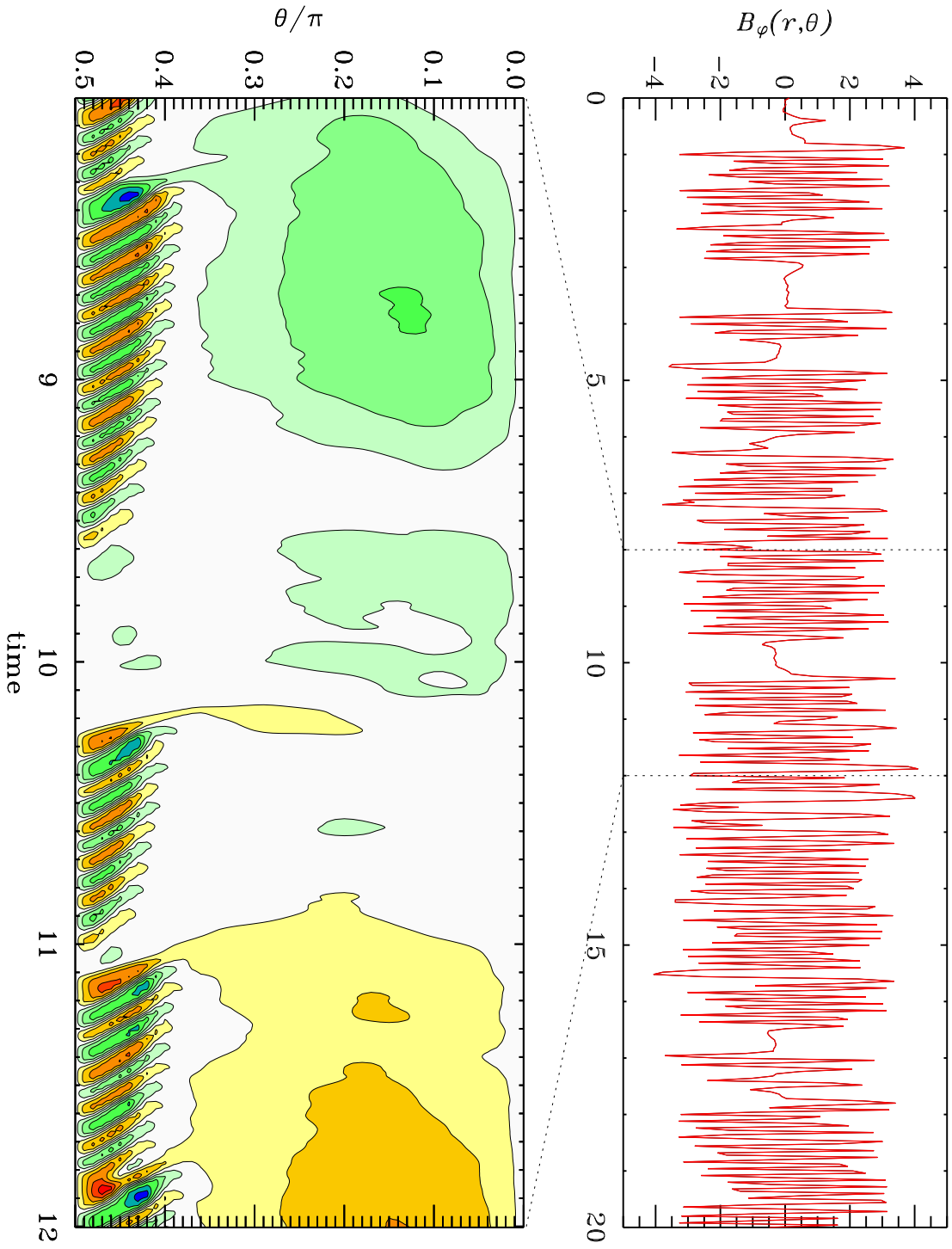

Figure 10.20: Intermittency in a dynamo model based on flux tube instabilities (cf. §10.4.2). The top panel shows a trace of the toroidal field, and the bottom panel is a butterfly diagram covering a shorter time span including a quiescent phase at $9.6 \lesssim t \lesssim 10.2$, and a "failed Minimum" at $t \simeq 11$. Figure produced from numerical data kindly provided by M. Ossendrijver.

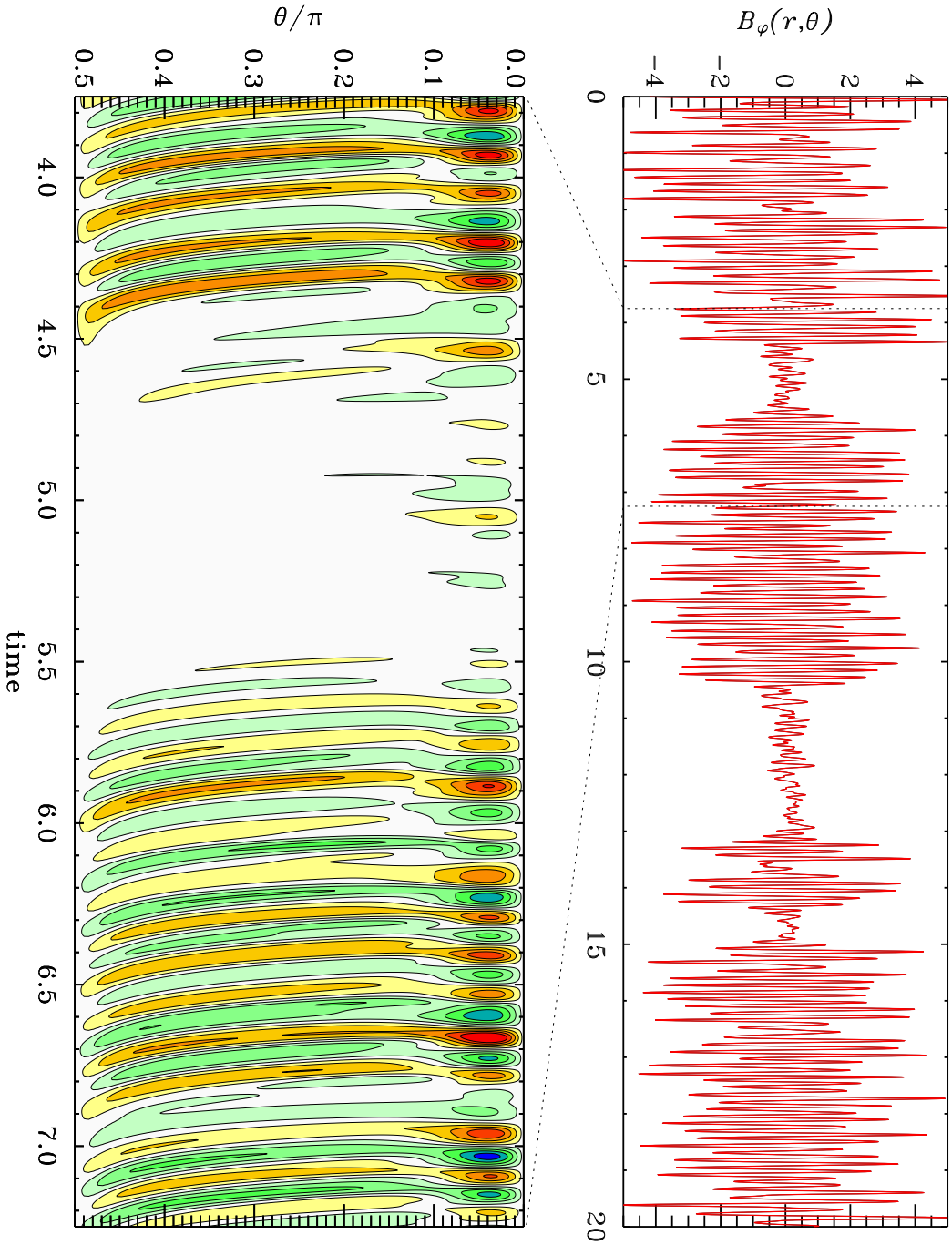

Figure 10.21: Intermittency in a dynamo model based on the Babcock-Leighton mechanism (cf. §10.3). The top panel shows a trace of the toroidal field sampled at $(r, \theta) = (0.7, \pi/3)$. The bottom panel is a time-latitude diagram for the toroidal field at the core-envelope interface. Numerical data from the Charbonneau et al. (2004) paper cited in the bibliography.

10.6 Predicting future cycles

Over the past decade, the prediction of solar eruptive events and their geomagnetic impacts, known as **space weather**, has become a Very Big Business. Even then, the prediction of the overall level of solar activity is also of interest, as it could be useful, among other things, to the planning of space missions and interplanetary travel. The understanding and prediction of activity levels on timescales decadal and longer is becoming known as **space climate**, and its primary data are the time series of sunspot numbers, and proxies such as the radioisotopes records.

One "hot" prediction problems, lying at the boundary of space weather and space climate, is the forecasting of the characteristic of the next solar activity cycle, which usually means the timing and amplitude of the cycle as measured in the sunspot number time series (see Fig. 6.5).

It is of course possible to treat this prediction problem as an exercice in time series analysis and forecasting, without any physical input. The SSN time series is just a time series, and it can be extended using a number of techniques coming from statistics (spectral analysis, wavelets, etc) or dynamical system theory (such as attractor reconstruction). We will focus here instead on prediction schemes based, in one form or another, on dynamo models.

In light of what we have learned in this chapter, we know we are facing a number of difficulties in trying to use dynamo models to forecast the solar cycle. A basic list of questions that need to be answered (excluding technical details for the time being) should include, at the very least, the following:

1. What type of dynamo powers the solar cycle: $\alpha\Omega$, $\alpha^2\Omega$, interface, Babcock-Leighton, etc.?

2. Which mechanism is driving duration and amplitude fluctuations: stochastic forcing, nonlinear modulation due to the Lorentz force, or time delay, etc.?

3. How do we "predict" sunspot number from a dynamo solution which describes the spatiotemporal evolution of just the diffuse, large-scale magnetic field?

These important questions notwithstanding, we have learned some important things that are useful in the present context. To start with, the dynamo feeds on the existing magnetic field, therefore trying to forecast the next cycle using characteristics of the current cycle (and maybe recent past cycles as well) is definitely justified. Problem 10.4 below lets you explore the performance of some very simple cycle forecasting schemes based on this notion.

Some recent solar cycle amplitude forecasts have used models of the type considered in this chapter, more specifically those of the Babcock-Leighton variety, in conjunction with crude formulations of data assimilation of surface magnetic field observations (see references cited in the bibliography). The current state of things is that forecasting models that appear extremely similar, except at the level of what one would usually consider modelling details, manage to produce forecasts for cycle 24 that are at opposite ends of the spectrum of cycle 24 predictions. In the context of Babcock-Leighton models, the overall approach is definitely viable in principle, since the solar surface magnetic field is that which will serve as seed to produce the sunspot-generating toroidal component of the next cycle. The one thing that the few recent model-based forecasting attempts have demonstrated beyond any doubts is that modelling details matter. Coming years will likely see progress on this front. To be continued!

Problems:

1. Suppose that the "**u**" in eq. (10.47) is just the differential rotation. Retaining the assumption fo axisymmetry for the large-scale flows and field, find the conditions under which eq. (10.48) does result from the substitution of eq. (10.47) into the ϕ-component of the momentum equation.

2. Consider the iterative map resulting from the use of a simple parabola for the "Babcock-Leighton function" introduced in §10.5.3:

$$p_{n+1} = \gamma p_n^2 (1 - p_n) \ ,$$

where γ is the map parameter;

   (a) Find the value of γ corresponding to the critical dynamo number for this map;

   (b) Find the values of gamma at which the first two period-doubling bifurcations take place.

   (c) Reconstruct the bifurcation diagram equivalent to that plotted on Fig. 10.19A for the "double-error-function" map. How similar are the two diagrams?

3. Sticking with the iterative map of the preceding problem, add now a low amplitude noise to the RHS of the map equation; this could be a random number uniformly distributed in the range $[-\varepsilon, \varepsilon]$, with $\varepsilon \ll 1$, chosen anew at each iteration of the map.

   (a) Pick a few γ values covering the singly-periodic range of the map, and a small value of ε ($= 0.1$, say); can you produce a Gnevyshev-Ohl-type effect in this way? Does this work at all values of γ?

   (b) Now introduce a random fluctuation in the map parameter γ, so that it covers the range going from singly-periodic to chaotic. You now have two distinct sources of fluctuations in the map. Do runs for increasing values of the additive noise magnitude ε. Find the intermittency threshold, i.e., the value of ε above which the iterate sequences varies irregularly between active and quiescent states.

4. This problem lets you explore some "brain-dead" prediction schemes for the solar cycle amplitude; the scary thing is that they don't do very much worse than much fancier and complicated schemes... Your starting point is the time series of sunspot number, either in the form of yearly mean values of smoothed monthly means (see Problem 6.2 for instructions on how to get a hold of these). Let's define the amplitude A_n of cycle n as the peak value.

   (a) The simplest forecasting scheme is to predict that the cycle amplitude will be equal to its average value over the past N cycles, where N is a relatively small number. Compute the r.m.s. prediction error made with this scheme for $N = 1$, $N = 2$ and $N = 3$.

   (b) The Gnevyshev-Ohl rule would suggest that a better predictor could be $A_n = A_{n-2}$; try this and see how it compares to the three predictors considered in (a).

   (c) This one calls upon your originality of thinking; try to design a simple predictor, similar in style to the ones considered in (a) and (b), that can do better.

   (d) Use all the above predictors to forecast the amplitude of upcoming cycle 24.

Bibliography:

A lot of the material in §§10.2, 10.3 10.4 and 10.5 is adapted from the following recent review paper:

Charbonneau, P., 2005, *Liv. Rev. Sol. Phys.*, **2**,

which is available online at

`http://solarphysics.livingreviews.org/Articles/lrsp-2005-2/`

See also these other recent review papers:

Ossendrijver, M. A. J. H., *Astron. Astrophys. Rev.*, **11**, 287–367 (2003).
Hoyng, P., "The field, the mean and the meaning", in *Advances in nonlinear dynamos*, The Fluid Mechanics of Astrophysics and Geophysics, **8**, eds. A. Ferriz-Mas & M. M. Jiménez, 1–36 (2003).

The technical literature on dynamo models of the solar cycle is truly immense. There are many hundreds of noteworthy papers out there! Those included below are just meant to be good entry points for those wishing to pursue in greater depth topics covered in this chapter. Mean-field models for solar (and planetary) dynamos were first discussed by

Steenbeck, M., & Krause, F. 1969, *Astr. Nach.*, **291**, 49.

The following is a very short list of "classics" that, in my opinion, are still well worth reading:

Lerche, I., & Parker, E.N. 1972, *Astrophys. J.*, **176**, 213,
Yoshimura, Y. 1975, *Astrophys. J.*, **201**, 740,
Ivanova, T.S., & Ruzmaikin, A.A. 1976, *Sov. Astron.*, **20**, 227,
Stix, M. 1976, *Astron. Ap.*, **47**, 243,
Rüdiger, G., and Brandenburg, A., *Astron. Astrophys.*, **296**, 557-566 (1995),
Moss, D., and Brooke, J. M., *Month. Not. R. Astron. Soc.*, **315**, 521-533 (2000).

On the impact of meridional circulation on dynamo waves, see

Roberts, P.H., & Stix, M., *Astron. Astrophys.*, **18**, 453 (1972),
Choudhuri, A.R., Schüssler, M., & Dikpati, M., *Astron. Astrophys.*, **309**, L29 (1995),
Küker, M., Rüdiger, G., and Schulz, M., *Astron. Astrophys.*, **374**, 301-308 (2001).

The meridional circulation profile described in §10.1 is the creation of

van Ballegooijen, A.A., & Choudhuri, A.R. 1988, *Astrophys. J.*, **333**, 965.

On α-quenching, standard versus catastrophic:

Blackman, E.G., and Field, G.B., *Astrophys. J.*, **534**, 984-988 (2000)
Cattaneo, F., and Hughes, D., *Phys. Rev. E*, **54**, R4532-R4535 (1996)
Durney, B.R., De Young, D.S., and Roxburgh, I.W., *Solar Phys.*, **145**, 207-225 (1993)
Rüdiger, G., and Kitchatinov, L.L., *Astron. Astrophys.*, **269**, 581-588 (1993).

On interface dynamos, see

Charbonneau, P., and MacGregor, K.B., *Astrophys. J.*, **473**, L59-L62 (1996)
MacGregor, K.B., and Charbonneau, P., *Astrophys. J.*, **486**, 484-501 (1997)
Parker, E.N., *Astrophys. J.*, **408**, 707-719 (1993)
Zhang, K., Chan, K. H., Zou, J., Liao, X., and Schubert, G., *Astrophys. J.*, **596**, 663-679 (2003),
Petrovay, K., & Kerekes, A., *Month. Not. R. Astron. Soc.*, **351**, L59 (2004).

What is now refered to as Babcock-Leighton solar-cycle models go back to the following three seminal papers by H. Babcock and R. Leighton:

Babcock, H.W. 1961, *Astrophys. J.*, **133**, 572,
Leighton, R.B. 1964, *Astrophys. J.*, **140**, 1547,
Leighton, R.B. 1969, *Astrophys. J.*, **156**, 1.

Although some details of the model are different, the 2D surface simulations described in §10.3.1 basically follow

Wang, Y.-M., Nash, A.G., & Sheeley, N.R. Jr 1991, *Science*, **245**, 712,
Wang, Y.-M., & Sheeley, N.R. Jr 1991, *Astrophys. J.*, **375**, 761.

but on this general topic of surface magnetic flux evolution, see also:

Baumann, I., Schmitt, D., Schüssler, N., and Solanki, S., *Astron. Astrophys.*, **426**, 1075-1091 (2004).

The formulation of the Babcock-Leighton solar cycle model of §10.3 is identical to

Dikpati, M., & Charbonneau, P. 1999, *Astrophys. J.*, **518**, 508.

For different modeling approaches, see

Wang, Y.-M., & Sheeley, N.R. Jr, & Nash, A.G. 1991, *Astrophys. J.*, **383**, 431,
Durney, B.R. 1995, *Solar Phys.*, **160**, 213,
Durney, B.R. 1997, *Astrophys. J.*, **486**, 1065.
Nandy, D., and Choudhuri, A. R. 2001, *Astrophys. J.*, **551**, 576-585.

The latter paper, in particular, explores the correspondence between Durney's discrete eruption approach, and the mean-field-like formulation used in §10.3.

On the "tachocline α-effect" dynamo model described in §10.4.1, and associated stability analyses, begin with:

Dikpati, M., and Gilman, P. A., *Astrophys. J.*, **559**, 428-442 (2001),
Dikpati, M., Gilman, P. A., and Rempel, M., *Astrophys. J.*, **596**, 680-697 (2003),
Gilman, P. A., and Fox, P. A., *Astrophys. J.*, **484**, 439-454 (1997).

And for the "flux tube α-effect" dynamo model of §10.4.2, and associated stability analyses, try first:

Ferriz-Mas, A., Schmitt, D., and Schüssler, M., *Astron. Astrophys.*, **289**, 949-956 (1994),
Ossendrijver, M. A. J. H., *Astron. Astrophys.*, **359**, 1205-1210 (2000).

On the effects of stochastic forcing on various dynamo models, start with:

Charbonneau, P., and Dikpati, M., *Astrophys. J.*, **543**, 1027-1043 (2000),
Choudhuri, A. R., *Astron. Astrophys.*, **253**, 277-285 (1992),
Hoyng, P., *Astron. Astrophys.*, **272**, 321-339 (1993),
Mininni, P., and Gomez, D.O., *Astrophys. J.*, **573**, 454-463 (2002),
Moss, D., Brandenburg, A., Tavakol, R., and Tuominen, I., *Astron. Astrophys.*, **265**, 843-849 (1992),
Ossendrijver, M. A. J. H., and Hoyng, P., *Astron. Astrophys.*, **313**, 959-970 (1996).

The following offer a good sample of the possible amplitude and parity modulation behaviors in nonlinear (sometimes non-kinematic) mean-field dynamo models:

Brooke, J. M., Moss, D., and Phillips, A., *Astron. Astrophys.*, **395**, 1013-1022 (2002),
Küker, M., Arlt, R., and Rüdiger, R., *Astron. Astrophys.*, **343**, 977-982 (1999),
Sokoloff, D., and Nesme-Ribes, E., *Astron. Astrophys.*, **288**, 293-298 (1994),
Tobias, S. M., *Astron. Astrophys.*, **322**, 1007-1017 (1997),
Bushby, P.J., *Month. Not. R. Astron. Soc.*, **371**, 772 (2006),
Rempel. M., *Astrophys. J.*, **647**, 662 (2006).

On time delay and its consequences for Babcock-Leighton dynamo models, see:

Charbonneau, P., *Solar Phys.*, **199**, 385-404 (2001),
Charbonneau, P., St-Jean-Leblanc, C., and Zacharias, P., *Astrophys. J.*, **619**, 613-622 (2005).

The following offers a few good entry points in the literature on intermittency in various types of dynamo models:

Charbonneau, P., Blais-Laurier, G., and St-Jean-Leblanc, C., *Astrophys. J.*, **616**, L183-L186 (2004),
Covas, E., and Tavakol, R., *Phys. Rev. E*, **60**, 5435-6645 (1999),
Ossendrijver, M. A. J. H., *Astron. Astrophys.*, **359**, 364-372 (2000),

Schmitt, D., Schüssler, M., and Ferriz-Mas, A., *Astron. Astrophys.*, **311**, L1-L4 (1996),
Tworkowski, A., Tavakol, R., Brandenburg, A., Brooke, J.M., Moss, D., and Tuominen, I., *Month. Not. R. Astron. Soc.*, **296**, 287–295 (1998).

Cycle prediction is a topic that has generated a massive literature, which often stands closer to statistical black magic than physics. A good review paper is

Hathaway, D.H., Wilson, R.M., & Reichmann, E.J., *J. Geophys. Res.*, **104**, 22375 (1999).

On the use of dynamo models for cycle prediction, see

Schatten, K.H., Scherrer, P.H., Svalsgaard, L., & Wilcox, J.M., *Geophys. Res. Lett.*, **5**, 411,
Dikpati, M., DeToma, G., & Gilman, P.A., GRL33L05102 (2006),
Choudhuri, A.R., Chatterjee, P., & Jiang, J., *Phys. Rev. Lett.*, **98**, 131103 (2007),

as well as

Bushby, P., & Tobias, S.M., *Astrophys. J.*, **661**, 1289 (2007).

This last paper is an illuminating criticism of the idea of using nonlinear dynamo models for cycle amplitude forecasting. Keep in mind, however, that the two forecasting models cited above (1) are *not* operating in a chaotic regime, and (2) achieve their forecasting not just through direct numerical simulation, but